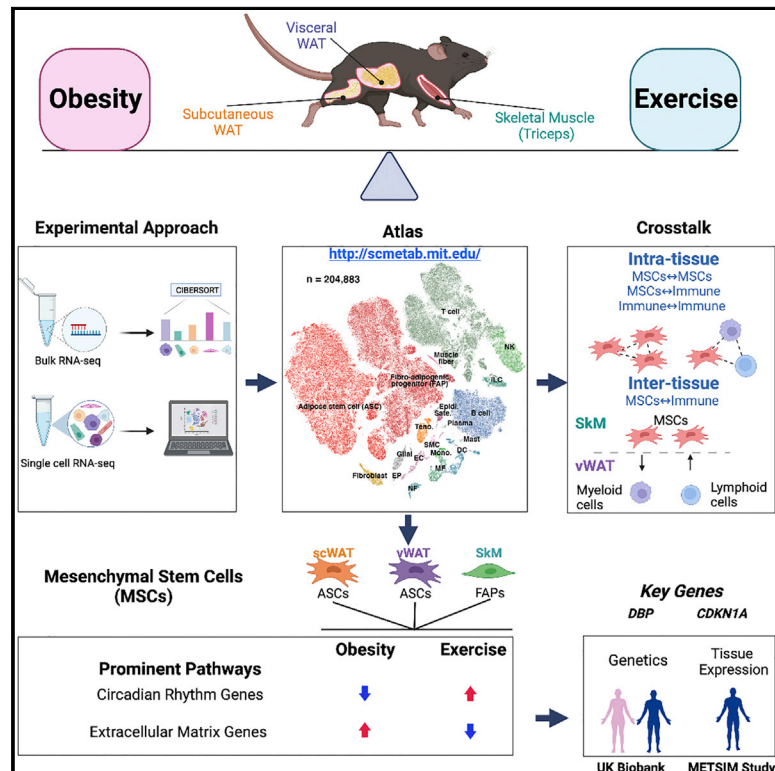


Cell Metabolism

Single-cell dissection of the obesity-exercise axis in adipose-muscle tissues implies a critical role for mesenchymal stem cells

Graphical abstract



Authors

Jiekun Yang, Maria Vamvini, Pasquale Nigro, ..., Kevin Grove, Laurie J. Goodyear, Manolis Kellis

Correspondence

laurie.goodyear@joslin.harvard.edu (L.J.G.), manoli@mit.edu (M.K.)

In brief

In this paper, Yang et al. provide a high-quality single-cell atlas of obesity-exercise interactions in subcutaneous and visceral white adipose tissue and skeletal muscle in mice. It uncovers a previously underappreciated role of mesenchymal stem cells in the response to obesity and exercise training in these three tissues.

Highlights

- Exercise-obesity single-cell atlas in two white adipose depots and skeletal muscle
- Exercise and obesity have opposite effects on ECM and circadian rhythmicity genes in MSCs
- Within- and multi-tissue crosstalk in exercise and obesity centered around MSCs
- Genes with large exercise effects in MSCs correlate with human metabolic traits



Resource

Single-cell dissection of the obesity-exercise axis in adipose-muscle tissues implies a critical role for mesenchymal stem cells

Jiekun Yang,^{1,2,9} Maria Vamvini,^{3,9} Pasquale Nigro,^{3,9} Li-Lun Ho,^{1,2} Kyriakitsa Galani,^{1,2} Marcus Alvarez,⁴ Yosuke Tanigawa,^{1,2} Ashley Renfro,^{1,2} Nicholas P. Carbone,³ Markku Laakso,^{6,7} Leandro Z. Agudelo,^{1,2} Päivi Pajukanta,^{4,5} Michael F. Hirshman,³ Roeland J.W. Middelbeek,³ Kevin Grove,⁸ Laurie J. Goodyear,^{3,*} and Manolis Kellis^{1,2,10,*}

¹Computer Science and Artificial Intelligence Laboratory, Massachusetts Institute of Technology, Cambridge, MA, USA

²Broad Institute of MIT and Harvard, Cambridge, MA, USA

³Section on Integrative Physiology and Metabolism, Joslin Diabetes Center, Harvard Medical School, Boston, MA, USA

⁴Department of Human Genetics, David Geffen School of Medicine at UCLA, University of California, Los Angeles, Los Angeles, CA, USA

⁵Institute for Precision Health, David Geffen School of Medicine at UCLA, University of California, Los Angeles, Los Angeles, CA, USA

⁶Institute of Clinical Medicine, Internal Medicine, University of Eastern Finland, Kuopio, Finland

⁷Department of Medicine, Kuopio University Hospital, Kuopio, Finland

⁸Novo Nordisk Research Center, Seattle, WA, USA

⁹These authors contributed equally

¹⁰Lead contact

*Correspondence: laurie.goodyear@joslin.harvard.edu (L.J.G.), manoli@mit.edu (M.K.)

<https://doi.org/10.1016/j.cmet.2022.09.004>

SUMMARY

Exercise training is critical for the prevention and treatment of obesity, but its underlying mechanisms remain incompletely understood given the challenge of profiling heterogeneous effects across multiple tissues and cell types. Here, we address this challenge and opposing effects of exercise and high-fat diet (HFD)-induced obesity at single-cell resolution in subcutaneous and visceral white adipose tissue and skeletal muscle in mice with diet and exercise training interventions. We identify a prominent role of mesenchymal stem cells (MSCs) in obesity and exercise-induced tissue adaptation. Among the pathways regulated by exercise and HFD in MSCs across the three tissues, extracellular matrix remodeling and circadian rhythm are the most prominent. Inferred cell-cell interactions implicate within- and multi-tissue crosstalk centered around MSCs. Overall, our work reveals the intricacies and diversity of multi-tissue molecular responses to exercise and obesity and uncovers a previously underappreciated role of MSCs in tissue-specific and multi-tissue beneficial effects of exercise.

INTRODUCTION

Regular physical exercise is a well-established intervention to prevent and treat people with obesity and diabetes (Kirwan et al., 2017). Determining the molecular mechanisms mediating the beneficial effects of exercise can lead to the identification of biomarkers and therapeutic targets (Sanford et al., 2020). However, this has been a challenging task because exercise is a complex physiological stimulus that induces beneficial adaptations to different organ systems by altering expression of key genes and proteins. We hypothesize that this occurs by directly impacting heterogeneous cell types within individual tissues and by modulating intra- and inter-tissue communication. Here, taking advantage of recent single-cell technologies and advancements in computational biology, we address the challenge by simultaneously investigating responses to exercise and obesity on the molecular, cell-type-specific, and cross-tissue levels.

White adipose tissue (WAT) and skeletal muscle (SkM) are among the most dynamic endocrine organs impacted by obesity and exercise, and as such have been the focus of studies on the tissue level (Gonzalez-Gil and Elizondo-Montemayor, 2020; Leal et al., 2018; Nigro et al., 2021; Sakurai et al., 2013; Stanford et al., 2015; Takahashi et al., 2019). Subcutaneous and visceral WAT (scWAT and vWAT), the two major WAT depots, as well as SkM are highly heterogeneous tissues with complex structures consisting of different cellular components. Both WAT depots are composed of mature adipocytes and the stromal vascular fraction (SVF), which consists of multiple cell types including adipose stem cells (ASCs) and a variety of immune cells (Stenkula and Erlanson-Albertsson, 2018). SkM consists of myofibers, surrounded by connective tissue; MSCs, including satellite cells and fibro-adipogenic progenitors (FAPs); and immune cells (Camps et al., 2020; Dos Santos et al., 2020; Oprescu et al., 2020; Rubenstein et al., 2020). Dissection of WAT using



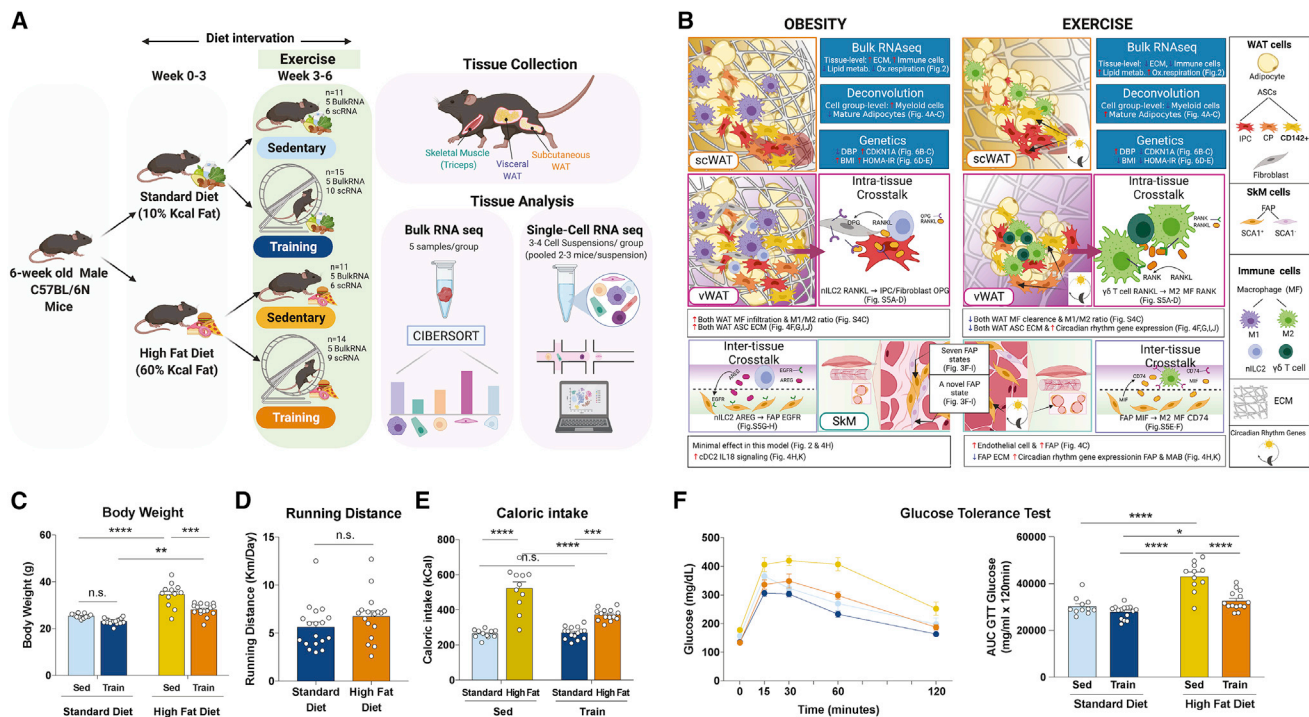


Figure 1. Study overview, highlighted results, and phenotypic responses

(A) Overview of the mouse study and tissue profiling.

(B) Summary of highlighted results. ECM, extracellular matrix.

(C–F) Body weight (C), running distance (D), caloric intake (E), and glucose tolerance test (GTT) result (F) in the four intervention groups.

* $p < 0.05$, ** $p < 0.01$, *** $p < 0.001$, **** $p < 0.0001$ by two-way ANOVA followed by Tukey multiple comparison tests. Data are represented as mean \pm SEM. AUC, area under curve; n.s., not significant. (A) and (B) were created with BioRender.com.

See also Figure S1.

single-cell or single-nucleus RNA sequencing has been presented in the context of obesity, cold exposure, or beta-adrenergic treatment but not following exercise interventions (Henriques et al., 2020; Rajbhandari et al., 2019; Sarvari et al., 2021; Vijay et al., 2020). In SkM, single-cell efforts have been limited compared to WAT and the existing studies have focused on SkM cell-type characterization and tissue regeneration (Camps et al., 2020; Dos Santos et al., 2020; Rubenstein et al., 2020). There have been no investigations of the beneficial effects of exercise to combat obesity at a single-cell resolution and spanning multiple tissues.

In this study, we dissect the opposing effects of exercise training and diet-induced obesity in scWAT, vWAT, and SkM at both tissue-level and single-cell resolution. Our results provide a reference atlas of obesity-exercise single-cell changes in metabolic tissues (Figures 1A and 1B; <http://scmetab.mit.edu/>) and reveal key roles for MSCs in potentially mediating tissue-specific and inter-tissue communication changes in response to obesity and exercise interventions.

RESULTS

Phenotypic response to diet-induced obesity and exercise and profiling of three metabolic tissues

We studied 6-week-old C57BL/6N male mice with diet-induced obesity and voluntary wheel running exercise training interven-

tions (Figure 1A; $n = 51$ across 4 groups). Phenotypically, high-fat diet (HFD) induced, and exercise attenuated, weight gain and glucose intolerance (Figures 1C and 1F). Diet did not significantly impact running distance (Figure 1D) and HFD mice consumed more calories, especially when sedentary (Figure 1E). Each statement is true for separate mouse cohorts studied for tissue- and single-cell-level experiments (Figures S1A–S1E). scWAT, vWAT, and SkM were collected and processed for transcriptomic profiling. For both bulk and single-cell assays, the major drivers of variation were tissue, diet, and exercise, but not batch (Figure S1F).

Tissue-level gene and pathway alterations by obesity-exercise across the three tissues

We found 1,386 tissue-level differentially expressed genes (DEGs) across all three tissues (568 in scWAT, 562 in vWAT, 256 in SkM; DESeq2-Negative-Binomial corrected $p < 0.05$) and all three pairwise intervention comparisons for “obesity” (HFD versus standard diet for sedentary), “training” (exercise training versus sedentary for standard diet), and “rescue” (exercise training versus sedentary for HFD; Tables 1 and S1). Gene ontology (GO) pathway enrichment and protein-protein interaction (PPI) analyses revealed common and distinct biological processes across interventions and tissues (Figures 2A–2D).

For the subset of DEGs identified in at least two comparisons in adipose tissues, nearly all (94%–95%) stemmed from

Table 1. Tissue-level DEGs with HFD and exercise training interventions

	Obesity (sed. HFD versus sed. std.)	Training (train std. versus sed. std.)	Rescue (train HFD versus sed. HFD)	Total
Common in WAT	up: 76 down: 75	up: 3 down: 0	up: 24 down: 17	195 (176 unique genes)
scWAT	up: 269 down: 223	up: 3 down: 0	up: 70 down: 62	627 (568 unique genes)
vWAT	up: 237 down: 241	up: 19 down: 28	up: 72 down: 133	730 (562 unique genes)
SkM	up: 0 down: 0	up: 64 down: 28	up: 147 down: 88	327 (256 unique genes)
Total	970	142	572	1,684 (1,386 unique genes)

Number of tissue-level DEGs with HFD and exercise training interventions. sed., sedentary; train, exercise training; std, standard diet.

opposite changes in obesity versus training/rescue (Figures 2A and 2B). This anti-correlation held for all genes (not only DEGs), with obesity versus rescue showing negative correlation in both depots (Pearson scWAT, $p < 10^{-10}$; vWAT, $p < 10^{-16}$), and obesity versus training anti-correlated in vWAT (Pearson, $p < 10^{-16}$; Figure S1G). Adipose-depot DEGs included both well-known and less-studied metabolism-associated genes. The latter included training/rescue increasing circadian rhythm regulators (*Dbp*, *Tef*, *Nr1d2*, and *Per3*), and training/rescue downregulating extracellular matrix (ECM) remodeling genes (*Thbs1* and *Sparc*). For SkM (Figure 2C), rescue/training upregulated 51 genes and downregulated 20 genes, including the fat metabolism repressor *Pdk4* (Kim et al., 2006) and the muscle-mass repressor *Asb2* (Davey et al., 2016). Rescue showed more DEGs than training ($n = 164$ versus 21), suggesting a more robust response of SkM to training under HFD than standard diet. Similar to WAT, training and rescue showed similar effect directions for most genes in SkM (Figure S1G).

Across tissues and interventions, DEGs clustered into biologically meaningful modules of interacting proteins (Figures 2D and S2). Rescue/training led to upregulation of fatty acid biosynthesis/beta-oxidation module and cellular respiration module, including oxidative phosphorylation, tricarboxylic acid (TCA) cycle, and reactive oxygen species (ROS) response. Rescue/training downregulated an immune module, including antigen presentation, neutrophil degranulation, immune cell migration, phagosome-related genes, and modules related to ECM and cell proliferation. Figure S2 summarizes the effect of each intervention on the genes comprising each module. For example, *Cdkn1a*, encoding a protein involved in cellular senescence, was downregulated by rescue in scWAT and vWAT (Figure S2). Taken together, these tissue-level results reveal specific genes and pathways that may mediate many of the beneficial effects of exercise training.

Single-cell atlas of metabolic tissues in obesity and exercise conditions

In addition to our tissue-level datasets, we generated a single-cell atlas of 204,883 cells for obesity-exercise interactions across the three tissues and the four intervention groups (Figure 3A). To capture low-abundance cell types (e.g., ASCs in WAT and FAPs in SkM), we used a single-cell library preparation

that enriched for stromal vascular fraction (SVF) instead of mature adipocytes in WAT and muscle fibers in SkM, parenchymal cells that are already well captured by tissue-level studies. We also included lymph nodes in scWAT to capture immune cells migrating between tissue and lymph nodes.

We annotated 22 cell types using marker gene expression in cell clusters (hierarchical and density-based) of non-linear embeddings (tSNE and UMAP) for dimensionality-reduced data (top 50 PCs; STAR Methods). These include (1) 3 types of stem cells, including ASCs, satellite cells, and FAPs; (2) 10 types of immune cells from both lymphoid and myeloid lineages; (3) 2 types of connective cells, including tenocytes in SkM and fibroblasts primarily in vWAT; (4) 2 types of muscle cells, including muscle fibers and smooth muscle cells; and (5) 4 additional cell types including endothelial, epithelial, epididymis, and glial cells (Figure 3A). Within each cell type, our analysis revealed subclusters driven by tissue provenance (Figure 3B; Table S2) and to a lower degree by intervention group (Figure 3C). Sub-clustering revealed 42 cell subtypes/states for 11 of the 22 cell types, including 3 ASC states, namely interstitial progenitor cell (IPC), committed preadipocyte (CP), and CD142+ ASC (Table S3). Two-dimensional embeddings of each tissue showed clear distinctions of these cell subtypes/states (Figure S3A).

Molecular signatures of depot-specific ASC states

We evaluated WAT ASC transcriptional diversity as a marker of differentiation potential (Figure 3D). The robustness of this concept was demonstrated in the CytoTRACE framework, which showed that transcriptional diversity decreases during differentiation (Gulati et al., 2020). For vWAT, we confirmed that IPCs show increased transcriptional diversity, consistent with their earlier differentiation state (Merrick et al., 2019). In scWAT, however, CPs and CD142+ cells showed increased transcriptional diversity, which may be related to their being *trans*-differentiation and de-differentiation potential (Ghaben and Scherer, 2019). We performed pseudotime trajectory analysis (Qiu et al., 2017) and selected the starting point of the trajectory (IPCs) based on previous experimental evidence (Merrick et al., 2019). The predicted pseudotime depicted a trajectory from IPCs to CPs and CD142+ cells in both WAT depots (Figure S3B).

We sought co-expressed regulator/target-gene combinations (regulons) for each ASC state to gain insights into their

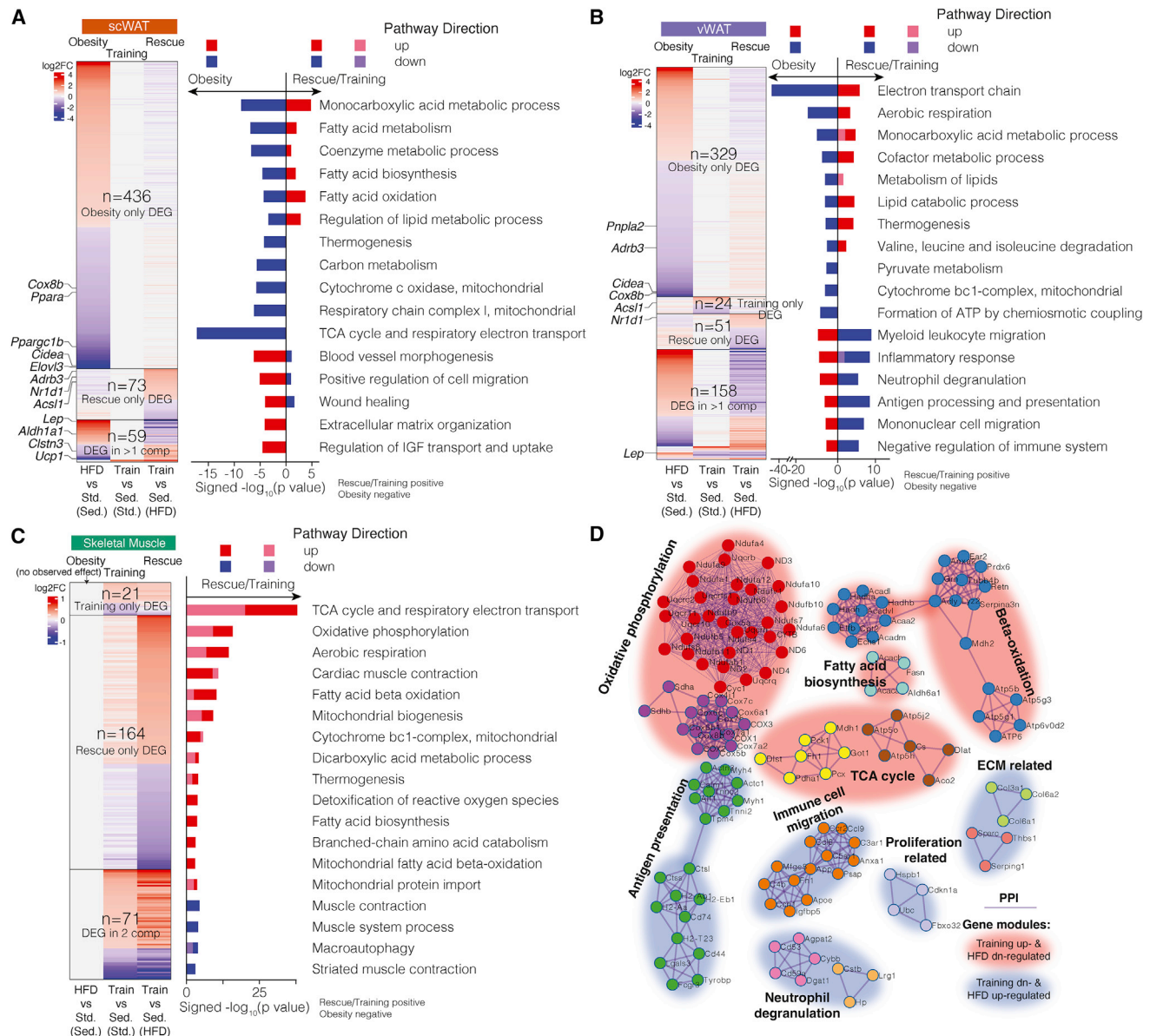


Figure 2. Tissue-level transcriptomic responses

(A–C) Genes (heatmap) and pathways (bar plot) that are significantly differentially expressed and enriched across three comparisons: “obesity,” “training,” and “rescue” in scWAT (A), vWAT (B), and SkM (C). The gene heatmap is colored by log₂ fold change. The pathway bar plot is colored by pathway direction in the three comparisons (red/pink, upregulated; blue/purple, downregulated). x axis of the bar plot shows $-\log_{10}$ p value with rescue/training pathways being positive and obesity being negative. DEG, differentially expressed gene.

(D) Gene networks across selected DEGs from the three tissues that encode interacting proteins, clustered by protein-protein interactions with each cluster named by the most significantly enriched pathway. The cluster is colored by DEG direction with exercise training.

sed., sedentary; train, exercise training; std, standard diet.

See also [Figures S1](#) and [S2](#) and [Table S1](#).

gene-regulatory circuitries. We identified depot-shared as well as depot- and state-specific regulons ([Figure 3E](#)). Depot-shared regulons ([Figure 3E](#), blue) included established regulons Klf3 and Creb5 for IPCs, which are activated very early during adipogenesis ([Farmer, 2006](#); [Sue et al., 2008](#)); regulons Cebpa, Pparg, and Gsc for CPs, among which Cebpa and Pparg are the two principal adipogenic factors overseeing the terminal differentiation process ([Farmer, 2006](#)); and for CD142+ cells, a regulon

controlled by thyroid hormone receptor beta (Thrb). As for the depot- and state-specific regulons, IPC-highest Irx3 (lowest in CPs) in scWAT is consistent with its early-adipocyte-differentiation role ([Claussnitzer et al., 2015](#)). In vWAT pre-CPs, a state lying between IPCs and CPs, we identified two potential IPC-to-CP lineage commitment regulators. Foxc1 is implicated in progenitor cell identity maintenance ([Omatsu et al., 2014](#)), and Nfil3 is implicated in a circadian lipid metabolic program and regulating

lipid absorption and export (Wang et al., 2017). Overall, our single-cell data highlight depot-shared and depot-specific gene regulatory circuitries for different populations of ASCs and enable regulator prediction for early ASC differentiation in vWAT.

Seven distinct FAP states and a novel FAP population in SkM

We classified the ~55,000 FAPs into seven distinct cellular states using mouse and human markers (Camps et al., 2020; Oprescu et al., 2020; Rubenstein et al., 2020): (1) multipotent IPC_SkM, sharing IPC markers with WAT; (2) FAP_Cxcl14+; (3) FAP_Prg4+; (4) adipogenesis-regulating FAP_CD142+ cell similar to adipose tissue CD142+ cell (Camps et al., 2020); (5) FAP_post_injury representing an inflammatory post-injury-like state; (6) mesoangioblasts (MABs), marked by *Alpl*+; and (7) a previously unreported Sca1 population of FAPs, discussed in more detail below (Figure S3C). The first six subtypes were all positive for *Pdgfra*, *Cd34*, and *Ly6a* (Figure S3D). All seven subtypes were detectable in previous single-cell data (Dos Santos et al., 2020; Oprescu et al., 2020) (Figure S3E).

Surprisingly, while FAPs are usually defined using interchangeable combinations of the canonical markers *Pdgfra*+, *Cd34*+, and *Sca1*+, we found an FAP population negative for *Sca1* (Joe et al., 2010) (Figure S3D). Downregulation of *SCA1* occurs as cells differentiate along a particular lineage (Soliman et al., 2020). According to CytoTRACE differentiation prediction, *Sca1*– FAPs showed a more differentiated state (less transcriptional diversity) than *Sca1*+ FAPs (Figure 3F). Trajectory analysis (Qiu et al., 2017) confirmed the differentiated state of *Sca1*– FAPs with later pseudotime (Figure S3C). *Sca1*– FAPs expressed higher levels of collagen genes, which are pan-fibroblast markers, and *IL33*, which is known for its role in recruiting Tregs and ILC2s in non-lymphoid tissues to combat inflammation (Spallanzani et al., 2019) (Figure S3F). Thus, we hypothesize *Sca1*– FAPs as a population of fibrogenic progenitors differentiated from MSCs. We validated *Sca1*– FAPs for both triceps and gastrocnemius muscle by stringent fluorescence-activated cell sorting (FACS) and gating. We used qPCR to verify expression patterns of *Sca1*+ (*Pdgfra*, *Ly6a*, and *Dpt*) versus *Sca1*-marker genes (*Pdgfra* and *ApoE*), and lack of expression of endothelial cell (*Pecam1*), tenocyte (*Scx*), or glial cell markers (*Pip1*; Figures 3G, S3G, and S3H; Table S3). We visualized *Sca1*–

FAPs using RNA and immunofluorescence staining (Figures 3H and 3I). Based on marker gene expression, this FAP is similar to a population reported in heart (cardiac fibrogenic *Sca1*– cell) (Soliman et al., 2020) (Figure S3I), which was differentiated from *PDGFR α* + *Sca1*+ cells. This *Sca1*– population increased in post-myocardial infarction hearts with a pathogenic role in remodeling and arrhythmogenic cardiomyopathy. Interestingly, there was a trend for *Sca1*– FAP abundance to decrease in training leading to the hypothesis that exercise training downregulates SkM fibrosis through its effects on *Sca1*– FAPs.

Marker genes for the seven FAP states were enriched in shared and unique pathways (Figure 3J). Shared pathways across the seven states included core matrisome, matrisome associated, IGF transport and uptake, and aging, suggesting FAP as a key contributor to ECM (Chapman et al., 2017), IGF signaling (Giuliani et al., 2021), and aging (Ancel et al., 2019) in SkM. FAP state-specific signaling pathways and regulons supported their respective functions (Figures 3J and 3K). In *Sca1*– FAPs, we found *IL6*-mediated signaling pathways and the *Mafg* and *Cebpg* regulons, which are involved in the *IL6*-induced oxidative stress response (Forcina et al., 2019), highlighting a potential response of this population to *IL6* that is known to be released with muscle contraction (Lauritzen et al., 2013).

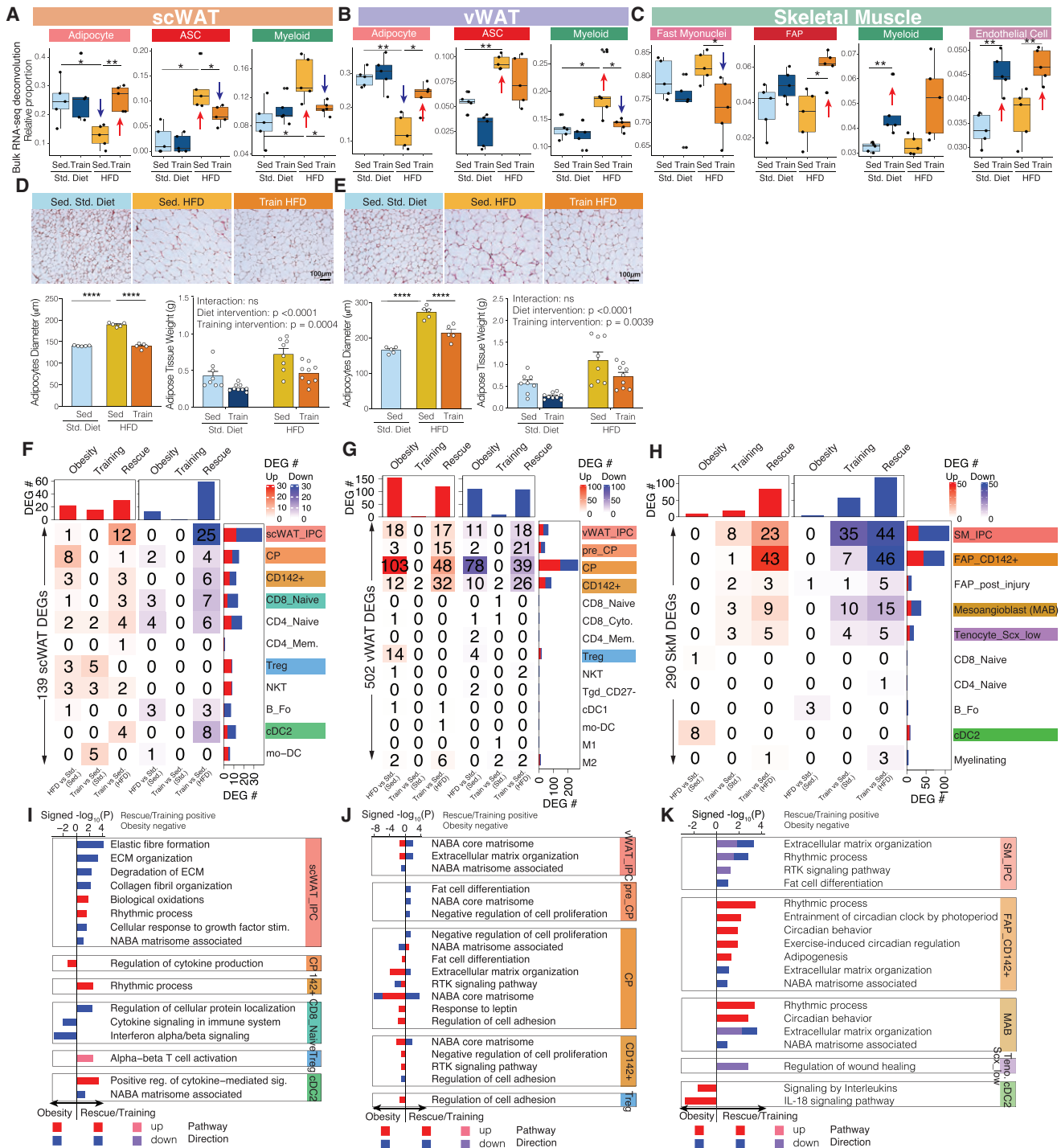
Cell-type and cell-state proportion changes in obesity and exercise across the three tissues

We also deconvolved (Newman et al., 2015) our tissue-level data using independent single-cell maps refined by manual curation (Dos Santos et al., 2020; Rajbhandari et al., 2019). As expected, deconvolution captured primarily high-abundance cell types (Table S2). We used these tissue-deconvolution results to characterize cell-type proportion changes in our three intervention comparisons. In both adipose tissues, HFD-induced obesity significantly decreased mature adipocytes and increased ASCs and myeloid cells (Figures 4A and 4B), consistent with increased adipocyte necrosis and macrophage infiltration in obesity-associated metabolic decline (Ghaben and Scherer, 2019). Exercise training reversed these effects in HFD, even though training alone showed no effect under standard diet conditions. Histology staining in both WAT depots showed that obesity significantly enlarged mature adipocyte size (adipocyte

Figure 3. Single-cell atlas and mesenchymal stem cell state characterization

- (A) Single-cell atlas of 204,883 cells across three tissues and four intervention groups. The tSNE plot is colored by cell type (warm colors, non-immune cell types; cold colors, immune cell types).
 (B and C) Single-cell atlas colored by tissue (B) and intervention group (C).
 (D) Re-clustering of ASCs in scWAT (left) and vWAT (right), colored by CytoTRACE-predicted differentiation stage (orange, less differentiated; gray, more differentiated). Ridge plots of individual ASC states are colored similarly.
 (E) Clustering of top ASC state-specific regulons (transcription factor with the number of regulated genes as a separate heatmap column) in scWAT (left) and vWAT (right). Shared regulons across the two depots are colored in blue. The heatmap is scaled by column.
 (F) Re-clustering of FAPs in SkM, colored by CytoTRACE-predicted differentiation stage (orange, less differentiated; gray, more differentiated). Ridge plots of individual FAP states are colored similarly.
 (G) FACS dot blot showing the sorting gates for *Sca1*+ and *Sca1*– FAPs from mouse triceps and gastrocnemius, with the percentages of the two populations labeled.
 (H) RNA staining of *Pdgfra* and *Ly6a* in triceps and gastrocnemius muscle.
 (I) Immunohistochemistry staining for *PDGFRA*, *SCA-1*, and *LAMA4* (a marker for muscle fibers) in gastrocnemius muscle.
 (J and K) Top pathways (J) and regulons (K) enriched in *Sca1*+ and *Sca1*– FAPs. The pathway heatmap is colored by $-\log_{10}$ p value. The regulon heatmap is colored by activity score.

See also Figure S3 and Tables S2 and S3.



(legend continued on next page)

hypertrophy) and increased tissue weight, which were both reversed by training (rescue; Figures 4D and 4E). In SkM, training and rescue decreased type II (fast) myonuclei and increased FAPs, myeloid cells, and endothelial cells (Figure 4C).

We also used our single-cell results to annotate changes in cell subtype/state proportions (Figures S4A–S4D; Table S2). In WAT across interventions, ASCs, macrophages, and T cells were the cell types with the most subtype/state proportion changes. In obesity, we found changes in vWAT specifically, with ASCs showing increased CD142+ cells, consistent with previous results (Merrick et al., 2019; Schwalie et al., 2018). Rescue once more reversed the change, decreasing CD142+ cells in vWAT (Figure S4B). In addition to ASCs, obesity both increased macrophage proportion and M1 (pro-inflammatory) versus M2 (anti-inflammatory) ratio in vWAT (Figure S4C). Rescue restored the M1/M2 ratio toward baseline. In lymphoid lineage there was an increase of Tregs and a decrease of NKT cells in obesity, changes reversed in rescue. Furthermore, there were similar changes of Tregs and NKT cells in training, suggesting that the beneficial effects of exercise training on lymphocytes occur regardless of diet. In SkM, training showed a tendency to decrease the ratio of Sca1– and Sca1+ FAPs, which suggests that training improved SkM physiology and decreased inflammation and fibrotic potential (Figure S4D).

Cell-type-specific transcriptomic changes highlight ECM remodeling and circadian rhythm gene expression in MSCs across the three tissues

We next used our single-cell data to infer cell-state-specific and cell-type-specific gene expression changes modulated by obesity and exercise training interventions. In WAT (Figures 4F and 4G; Table S4), we found 139 scWAT DEGs and 502 vWAT DEGs at the cell-state level, affecting primarily ASCs followed by T cells in both WAT depots. In ASCs, DEGs in IPCs and CPs accounted for 57% in scWAT and 59% in vWAT, indicating that IPCs and CPs are the ASC states most responsive to the interventions. Between the two fat depots, vWAT was affected the most by obesity, showing a 7.6-fold enrichment for DEGs (265 versus 35). In vWAT, rescue reversed ~12% of the obesity-regulated genes in ASCs, but 0% in T cells, indicating that obesity-induced immune dysregulation is potentially longer-lasting. In SkM, we identified 290 DEGs (13 obesity + 74 training + 203 rescue; Figure 4H; Table S4). Rescue led to more single-cell DEGs than obesity and training, consistent with our tissue-level results. Sca1+ FAPs showed the most DEGs, with IPC_SkM and FAP_CD142+ cell accounting for 81% of the Sca1+ FAP DEGs. Cell-type-level DEGs showed similar gene expression change patterns for the three tissues and the three phenotypic comparisons (Figures S4E–S4G).

In the three tissues, ECM-related pathways were upregulated by obesity and downregulated by training and rescue in scWAT IPCs, all four states of vWAT ASCs, and three Sca1+ FAP states (IPC_SkM, FAP_CD142+, and MAB; Figures 4I–4K; Table S4).

Excessive deposition of ECM has been observed with obesity in WAT to both provide structural support to the enlarged mature adipocytes and promote tissue fibrosis (Marcelin et al., 2017; Shao et al., 2021). In SkM, ECM is essential for muscle development, growth, repair, and mechanical support during exercise. These data support a significant role for ASCs in scWAT and vWAT and FAPs in SkM in regulating ECM remodeling in the context of obesity and exercise.

Circadian rhythm is another notable pathway regulated in all the three tissues, which was only observed in single-cell but not tissue-level data. The pathway was upregulated by training and rescue and enriched in FAPs in SkM and ASCs in WAT, suggesting a close link between exercise and circadian rhythmicity in these tissues (Figures 4I–4K; Table S4). Upstream regulator analysis revealed *Dbp*, *Tef*, and *Hlf*, three homologous PAR bZIP TFs sharing motif specificity (Yoshitane et al., 2019), as potential master regulators of these training-altered circadian pathways in specific MSC states (Figures S4H–S4J). These findings suggest that exercise training upregulates the circadian rhythm pathway through shared transcriptional regulators in MSCs of the three tissues.

Distinct cell-type-specific pathways regulated by exercise and obesity in each tissue

In scWAT, pathway analysis of the DEGs indicated that obesity downregulated type I interferon signaling and defense response in T cells, which suggests a shift from adaptive immune response to inflammation (Figure S4E; Table S4). Rescue was enriched in the prostaglandin synthesis and regulation pathway in ASCs, which included a downregulation of the expression of the prostaglandin degradation gene *Hpgd* by 1.5-fold (Figure S4E; Table S4). Downregulated *Hpgd* is associated with increased prostaglandin E₂ levels, which has been shown to help to maintain ASC self-renewal capacity and enhance immunomodulatory potency (Lee et al., 2016).

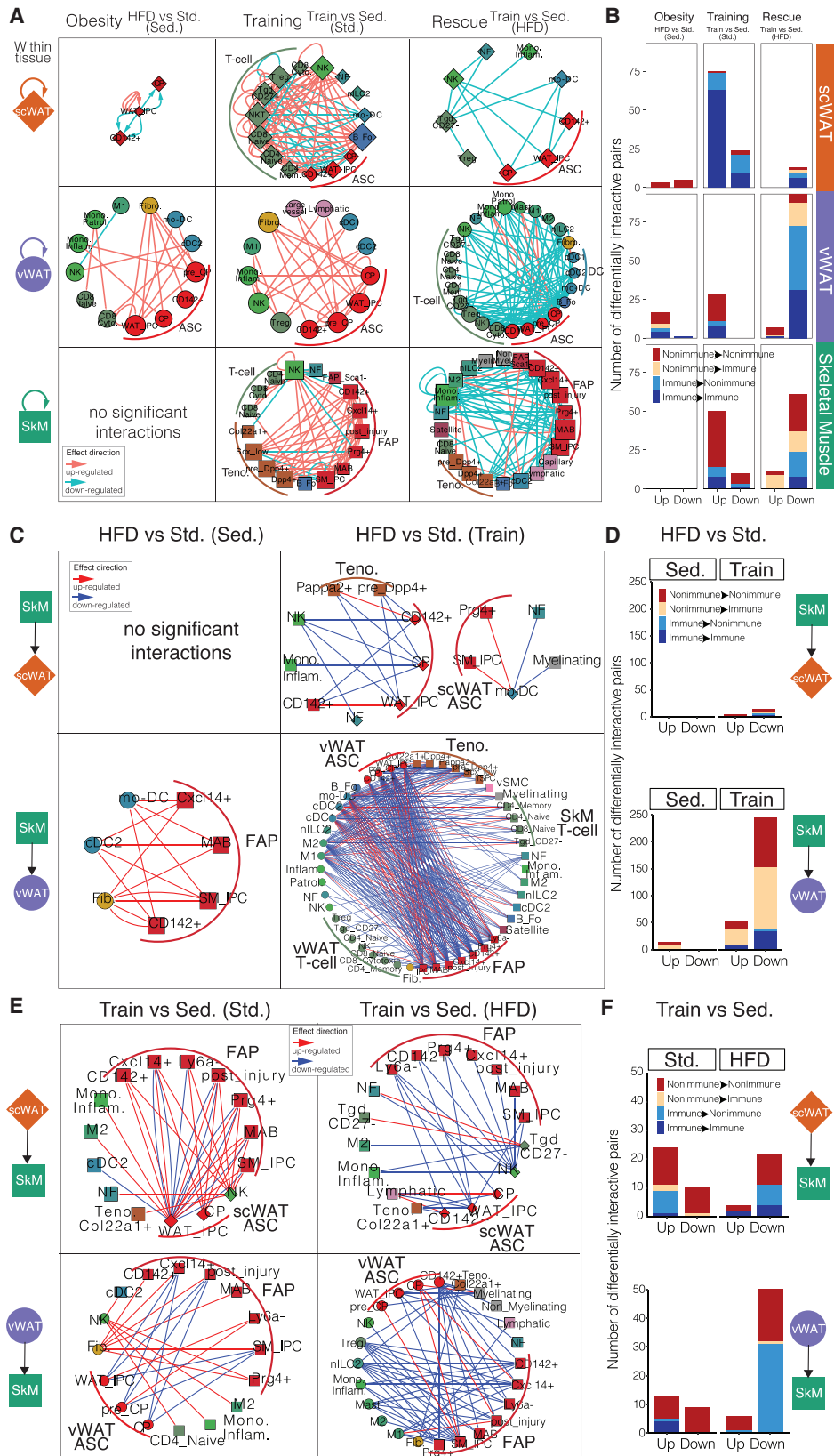
In vWAT, obesity upregulated and rescue downregulated two pathways that may mediate *de novo* adipogenesis in ASCs (Figure S4F; Table S4). One is the TGFβ1 stimulus response, an anti-adipogenic inflammatory molecule secreted from hypertrophic, dysfunctional adipocytes and known to inhibit adipocyte differentiation in mice and humans (Ghaben and Scherer, 2019). The second is ROS metabolic process, whose intracellular accumulation by mitochondrial respiration decreases preadipocyte differentiation and drives a pro-inflammatory and fibrotic phenotype (Joffin et al., 2021; Shao et al., 2021).

In SkM, obesity upregulated IL-18 and cytokine signaling pathways in DCs and rescue downregulated fat cell differentiation in FAPs (Figure S4G; Table S4). In myopathies and obesity, FAP adipogenesis has been reported to be involved in ectopic fat deposition (Jia and Sowers, 2019; Reggio et al., 2020). Rescue downregulated adipocyte differentiation, consistent with increased FAP CD142+ (Figure S4D), which inhibits

(I–K) Pathways (bar plot) that are significantly enriched in cell-state-specific DEGs across the three comparisons in scWAT (I), vWAT (J), and SkM (K). x axis of the bar plot shows $-\log_{10}$ p value with rescue/training pathways being positive and obesity being negative. The bars are colored by pathway direction in the three comparisons (red/pink, upregulated; blue/purple, downregulated).

* $p < 0.05$, ** $p < 0.01$, *** $p < 0.001$, **** $p < 0.0001$ by Wilcoxon rank-sum test (A–C) or by two-way ANOVA followed by Tukey multiple comparison tests (D and E). Data are represented as mean \pm SEM (D and E).

See also Figure S4 and Tables S2 and S4.



(legend on next page)

adipogenesis in SkM (Camps et al., 2020). In the immune compartment of SkM, obesity upregulated the IL-18 signaling pathway in conventional type 2 DCs, consistent with the IL-18 increase in DCs in inflammatory myopathies (Tucci et al., 2007).

DEGs identified using deconvolved tissue-level data were mostly regulated in opposite directions in obesity versus training/rescue (Figures S4K–S4M). The enriched pathways in both fat depots include lipid metabolism in mature adipocytes, ECM-related pathways and IGF transport and uptake in ASCs and myeloid cells, immune cell activation, regulation of inflammatory response, and monocyte chemotaxis in lymphoid and myeloid cells. In SkM, 44 out of the 50 tissue-deconvolved DEGs were found within fast myonuclei (Figure S4M).

Exercise training reprograms within- and cross-tissue cellular communication

Taking advantage of our high-resolution single-cell annotations, we used co-expression of interacting structure-based ligand-receptor pairs (Efremova et al., 2020) to predict pairwise cellular communication within and across tissues and interventions at both cell-type and cell-state levels (Figures 5 and S5; Table S5).

Within tissues, we observed MSCs function as self- and cross-regulating hubs of immune and non-immune cell types in obesity, training, and rescue comparisons (Figures 5A, 5B, S5A, and S5B). By comparing ranks of significant interactions overlapping intervention groups, we observed networks of differential interactions, including obesity upregulated non-immune interactions (ASC autocrine regulation in scWAT and fibroblast-ASC interactions in vWAT). RANK-RANKL-OPG triad showed a particularly interesting co-expression pattern change in response to HFD and exercise training in vWAT (Figures S5A, S5C, and S5D). RANK is the receptor among the three and encoded by *Tnfrsf11a*, RANKL is the ligand and encoded by *Tnfrsf11*, and OPG (osteoprotegerin) is the decoy receptor of RANKL and encoded by *Tnfrsf11b*. OPG was mostly expressed in ASC IPCs and fibroblasts, RANKL was highly expressed in nILC2s and CD27[−] Tgds, and RANK was expressed mainly in M2 macrophages (Figure S5C). Obesity increased OPG expression in fibroblasts and IPCs and RANKL expression in nILC2s while training and rescue decreased OPG expression (Figure S5D). Interestingly, RANKL expression in CD27[−] Tgd and RANK expression in M2 macrophages showed an opposite trend of changes in obesity versus training and rescue. This led us to hypothesize that HFD promoted interaction between RANKL in nILC2 and the decoy receptor OPG in fibroblast and IPCs, and on the contrary, exercise training induced a shift from this ligand-receptor interaction to interaction between RANKL from CD27[−] Tgd and RANK from M2 macrophage.

Across tissues, we performed slightly different comparisons to highlight physiologically meaningful directed communication changes between WAT and SkM with obesity and exercise training. Specifically, we compared ligand-receptor co-expression from SkM to WAT mediating the effect of obesity (HFD versus standard diet) in sedentary state or with exercise training. We performed a similar analysis from WAT to SkM comparing the training effect (training versus sedentary) under HFD or standard diet. We discovered that HFD effect with exercise training downregulated cross-tissue communication from non-immune cell states in SkM to immune cell subtypes in vWAT compared to HFD effect with the sedentary condition (Figures 5C and 5D). However, there is little such communication between SkM and scWAT. Conversely, training effect with HFD downregulated numerous crosstalk from immune cell subtypes in vWAT to non-immune cell states in SkM compared to training effect with standard diet (Figures 5E and 5F). The SkM non-immune cell states involved in the two-way interactions are primarily FAP states, while the immune cell subtypes differ for the ones receiving molecular signals from SkM with training versus the ones sending signals to SkM with HFD (Figures 5C–5F). Specifically training downregulated SkM FAP ligands with co-expressing receptors on DCs and macrophages in vWAT (Figures 5C and 5D). MIF-CD74 signaling is one such interaction, which was downregulated by exercise training from different SkM cell types including FAPs to M1 macrophages and cDC1s and cDC2s in vWAT, but slightly upregulated its interaction with M2 macrophages (Figures S5E and S5F). In turn, HFD downregulated interactions between ligands secreted from Tregs and nILC2s in vWAT and corresponding receptors on FAPs in SkM (Figures 5E and 5F). Expression of AREG secreted by Tregs and nILC2s in vWAT and its receptor EGFR on FAPs in SkM was co-downregulated by HFD (Figures S5G and S5H). AREG-EGFR signaling has been shown to play an important role in wound healing by regulating differentiation of fibroblasts to myofibroblasts and their proliferation in many diseases (Son et al., 2021). Based on our results, exercise training may dampen the HFD-induced profibrotic effect on SkM through regulation of the AREG-EGFR signaling axis between vWAT and SkM. More interestingly, although there are cell types expressing MIF within vWAT and cell types expressing AREG in SkM, we did not detect significant within-tissue interaction changes for these two ligand-receptor pairs with exercise, further indicating the importance of cross-tissue analysis in the context of obesity-exercise interaction.

Genetics of two exercise-training candidate genes in two independent large-scale human studies

To evaluate the human relevance of our results, we selected one gene that was upregulated and one that was

Figure 5. Within- and cross-tissue communication at cell-state level

(A) Within-tissue ligand-receptor networks across the three tissues and three comparisons. Cell states (nodes) are shaped by tissue (diamond, scWAT; circle, vWAT; square, SkM) and sized by outdegree. Ligand-receptor interactions (edges) are directed, from ligand to receptor, and colored by effect direction (pink, upregulated; blue, downregulated).

(B) The number of differentially interactive ligand-receptor pairs that are up- and downregulated across the three tissues and three comparisons at the cell-state level. Each bar is colored by whether the ligand or the receptor is from an immune or non-immune cell state.

(C and E) Cross-tissue ligand-receptor networks between a pair of tissues and in diet (C) or training (E) comparisons. The nodes and edges are formatted as in (A).

(D and F) The number of differentially interactive ligand-receptor pairs that are up- and downregulated between a pair of tissues and in diet (D) or training (F) comparisons at the cell-state level. The bars are colored as in (B).

See also Figure S5 and Table S5.

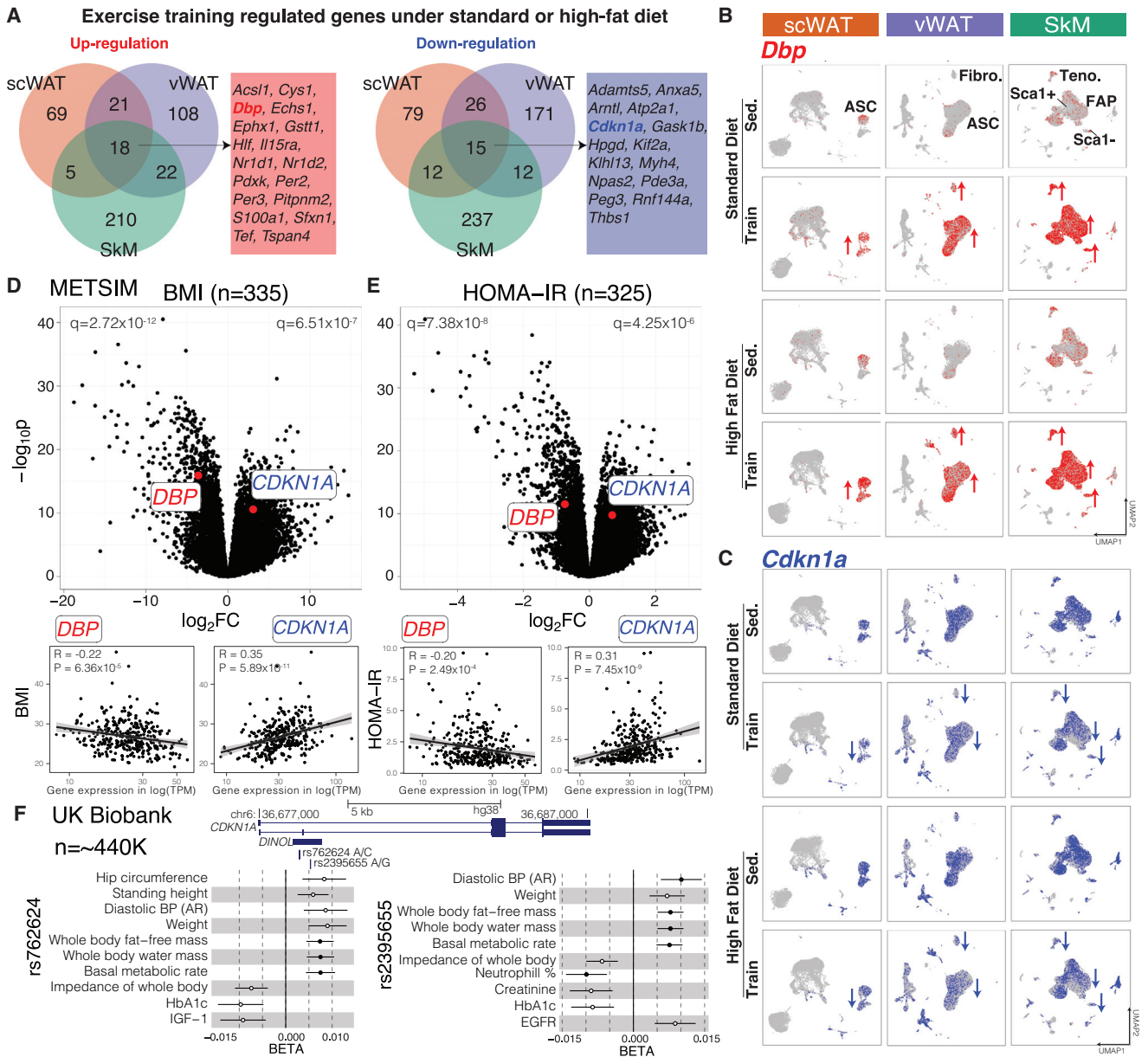


Figure 6. Two exercise-regulated genes (DBP and CDKN1A) in mice and humans

(A) Overlap of up- and downregulated genes by exercise training under standard or HFD across the three tissues in mice. (B and C) *Dbp* (B) and *CDKN1A* (C) expression across the three tissues and four intervention groups. Cell types with the most changes are labeled in the top panel. (D and E) *DBP* and *CDKN1A* association with BMI (D) and HOMA-IR (E) in scWAT of METSIM subjects. Genes (dots in upper plots) and subjects (dots in lower plots) are plotted. (F) Association of two SNPs (rs762624 and rs2395655) in *CDKN1A* with anthropometric and metabolic traits in UK Biobank. The meta-analyzed PheWAS summary statistics (BETAs with standard errors, $p < 1e-3$) are shown. The filled circles are significant after correction ($p < 1e-5$). PheWAS, phenome-wide association study; BP, blood pressure; AR, automated reading. See also Figure S6.

downregulated across all three tissues and tested anthropometric trait genetic associations in UK biobank (Sudlow et al., 2015) and human metabolic tissue expression changes in the Metabolic Syndrome in Men (METSIM) study (Laakso et al., 2017) (Figure 6A). Among the 18 commonly upregulated genes, we selected *Dbp* (Figure 6B), as it is a key regulator in diet/exercise-regulated circadian rhythm pathways and its homologs

Hlf and *Tef* were also upregulated in MSCs by exercise training. In humans, *DBP* showed a negative correlation with body mass index (BMI), homeostatic model assessment for insulin resistance (HOMA-IR), fasting serum insulin and glucose concentrations, C-reactive protein (CRP), and waist-hip ratio (WHR) adjusted for BMI, and a positive correlation with Matsuda insulin sensitivity index in METSIM (Figures 6D, 6E, and S6A–S6F),

demonstrating DBP's obesity and exercise relevance in human phenotypes.

Of the 15 commonly downregulated genes, we selected cell proliferation and senescence regulator *Cdkn1a*. *Cdkn1a* is downregulated by training/rescue primarily in MSCs in the three tissues as assessed using both bulk and single-cell methods (Figure 6C). In humans, *CDKN1A* showed a positive correlation with BMI, HOMA-IR, fasting insulin levels, CRP, and WHR adjusted for BMI and a negative correlation with Matsuda insulin sensitivity index in METSIM (Figures 6D, 6E, and S6A–S6F). The *CDKN1A* genetic locus contained two SNPs, one intronic (rs762624) and one missense (rs2395655) in linkage disequilibrium ($r^2 = 0.49$ in EUR), that were significantly associated with body weight, fat and fat-free mass, and basal metabolic rate in the UK Biobank (Figure 6F). The minor allele of both SNPs (C for rs762624 and G for rs2395655) showed protective associations with increased body fat-free mass, increased basal metabolic rate, and lower HbA1c. These SNPs are significant splicing quantitative trait loci (QTLs) for *CDKN1A* in METSIM, with the minor alleles increasing expression of a non-coding transcript isoform (long non-coding RNA, ENST00000462537.3; Figures S6G and S6H). These results suggest a potentially causal role for *CDKN1A* in human metabolic phenotypes, validating the human disease relevance of our results.

DISCUSSION

Our single-cell atlas with more than 200,000 cells and 53 annotated cell subtypes/states enabled identification of rare cell subtypes/states, notably MSC populations in three key metabolic tissues (scWAT, vWAT, and SkM). We computationally inferred the differentiation trajectory of ASCs and identified depot-shared and depot-specific regulons for the three ASC states in scWAT and vWAT (IPCs, CPs, and CD142+ cells). We identified seven distinct FAP states in SkM and validated one population of Sca1–FAPs as potential fibrogenic progenitors. By studying the three tissues using comprehensive and complementary single-cell, tissue-level, and tissue-deconvolution analyses, we determined two prominent gene programs, ECM and circadian rhythm, both of which were regulated in opposite directions by exercise and obesity in MSCs across the three tissues. We inferred intra-tissue communication changes between ASCs and immune cell subtypes in vWAT. We inferred inter-tissue crosstalk changes between FAPs in SkM and immune cell subtypes in vWAT (Figure 1B). With this study, we set the foundation for understanding the molecular changes and cell types mediating the systemic and heterogeneous effects of exercise on obesity in different tissues.

Our single-cell data indicate that at the pathway level, obesity and exercise training modulate gene expression related to ECM remodeling and circadian rhythm in specific MSC states in the three tissues. Obesity upregulated and exercise downregulated ECM-related pathways in MSCs. Notably, IPC is the only shared MSC state across the three tissues showing consistent ECM pathway regulation with obesity and exercise. Recently, others reported the presence of fibro-inflammatory progenitors in mouse WAT depots, which correspond to IPCs (Figure S3J), with a fibrogenic and inflammatory phenotype featuring ECM gene expression (Hepler et al., 2018; Shao et al., 2021). In

humans the frequency of a similar population of cells has been shown to be correlated not only with omental WAT (oWAT) fibrosis level but also with the severity of insulin resistance and type 2 diabetes (Marcelin et al., 2017). Our results suggest that obesity and exercise training could modulate the fibro-inflammatory phenotype of IPCs through ECM-related gene expression.

Another notable MSC-specific exercise-regulated pathway detected in our study was the circadian rhythm pathway, which was upregulated by exercise training across the three tissues. We identified *Dbp* and its homologs *Tef* and *Hlf* as potential master regulators of the upregulated rhythmic pathway. *Dbp* is a transcription factor with expression under circadian control (Zvonic et al., 2006) and has been reported to improve insulin sensitivity and enhance adipogenesis in pre-adipocytes of vWAT in mice and humans (Suzuki et al., 2019; Ushijima et al., 2020). Taken together, we hypothesize that training-induced increases in circadian rhythm gene expression via *Dbp* may contribute to hyperplasia in WAT. Our hypothesis is further supported by our analysis of a large human cohort where *DBP* expression in scWAT is negatively associated with BMI and HOMA-IR. Thus, training-induced circadian rhythm genes in mice and humans may function as MSC differentiation regulators, affecting whole-body metabolic functions.

Single-cell data also empowered us to look into cell-cell communication within and across tissues. Our within-tissue analysis of vWAT highlighted an interesting protein triad, RANK-RANKL-OPG. High serum OPG levels have been associated with metabolic disease in humans, while low OPG levels and high RANKL in rodents were associated with scWAT browning, *de novo* adipogenesis, and improved metabolic function of WAT (Matsuo et al., 2020). RANK is mostly expressed on M2 macrophages in our single-cell data, macrophages known to confer anti-inflammatory and beiging functions in WAT (Li et al., 2020b). We propose that exercise changes RANKL-OPG to RANKL-RANK interaction, which could recruit M2 macrophages or re-polarize macrophages into an M2 state in vWAT, and in this way promote anti-inflammatory and beiging effects.

Our cross-tissue analysis suggested directed ligand-receptor interactions between distinct vWAT immune cell types and SkM FAPs in response to obesity and exercise training. MIF-CD74 signaling was downregulated by exercise training from SkM FAPs to M1 macrophages and DCs in vWAT, but slightly upregulated its interaction with M2 macrophages in the same tissue. Downregulation of MIF-CD74 signaling on macrophages and DCs has been shown to restore antitumor immune response in cancer (Figueiredo et al., 2018) and reduce adipose tissue inflammation (Kim et al., 2015), which aligns with the notion that exercise training reduces chronic inflammation in vWAT through secreted cytokines from SkM. At the same time, MIF-CD74 interaction is known to play important roles in cell proliferation and survival by activating PI3K-Akt, NF- κ B, and AMPK pathways (Farr et al., 2020; Moon et al., 2013), suggesting a potential pro-survival role of the MIF-CD74 signaling axis for M2 macrophages in vWAT. As such, an intriguing hypothesis is that MIF secreted from SkM acts differently on distinct myeloid subtypes in vWAT and that M2 macrophages are regulated by both intra- (RANKL) and inter-tissue (MIF) signals.

In summary, we propose a previously underappreciated role of MSCs in response to obesity and exercise training in the three

tissues, mediated through alterations in their fibrogenic, inflammatory, and differentiation potentials. Exercise, as one of the most effective strategies to maintain a healthy body and mind, is increasingly understood to induce tissue-specific and shared adaptations in the context of many other diseases beyond obesity. There may be similar exercise-induced alterations of MSCs in other tissues and in a diverse set of disease and physiological contexts such as cancer and aging.

Limitations of study

In this study, we did not investigate additional physiological conditions including sex, age, and different training modalities, and our experiments were done using a mouse model and not human subjects. Our single-cell protocol enriched for cell types in SVF and resulted in limited observations in parenchymal cell types. For the cross-tissue communication analysis, although we restricted one of the two interacting partners being secretable and the interaction being non-integrin, orthogonal data types such as proteomics in the blood and experimental efforts using *in vitro* co-culturing systems and *in vivo* tracer approaches will be useful to fully resolve tissue crosstalk.

STAR★METHODS

Detailed methods are provided in the online version of this paper and include the following:

- **KEY RESOURCES TABLE**
- **RESOURCE AVAILABILITY**
 - Lead contact
 - Materials availability
 - Data and code availability
- **EXPERIMENTAL MODEL AND SUBJECT DETAILS**
- **METHOD DETAILS**
 - Animals, exercise, and sample collection
 - Bulk mRNA sequencing
 - Single-cell RNA sequencing
 - Histology
 - FACS-based cell isolation, RNA isolation and quantitative PCR
 - RNAscope LS Multiplex Fluorescent ISH assay
 - Immunohistochemistry assay
- **QUANTIFICATION AND STATISTICAL ANALYSIS**
 - Analysis of bulk mRNA-seq data
 - scRNA-seq data analysis
 - METSIM and UK biobank analysis
 - Other computational analyses and data processing remarks

SUPPLEMENTAL INFORMATION

Supplemental information can be found online at <https://doi.org/10.1016/j.cmet.2022.09.004>.

ACKNOWLEDGMENTS

We thank Minna Kaikkonen-Määttä for advice and feedback on the work, Stuart Levine for generating high-quality data and technical support, Carlos Castorena and Angie Bookout for discussions and feedback on the HFD and exercise training-regulated genes, Karen Mohlke for analysis advice on the

METSIM cohort, Charlie Whittaker for help with bulk 3' DGE data processing, and Julio Mantero for experimental support. This work was supported by Novo Nordisk Research Center (M.K. and L.Z.A.), R01DK099511 (L.J.G.), 5P30-DK-36836 (Joslin Diabetes Center), U24HG009446 (M.K.), and UG3NS115064 (M.K.). J.Y. was supported by T32-DK110919; M.V. by T32-DK007260, F32-DK126432, and Joslin Diabetes Center P&F; R.J.W.M. by K23-DK114550; Y.T. by R01HG008155 and R01AG067151; and P.P. and M.A. by R01HG010505 and R01DK132775.

AUTHOR CONTRIBUTIONS

This study was designed and directed by L.J.G. and M.K. M.V. and P.N. performed the mouse protocol. M.V., P.N., L.-L.H., and K. Galani collected the tissues. K. Galani performed the scRNA-seq experiment. J.Y. performed data processing and computational analysis. M.A. performed analysis in METSIM. M.L. and P.P. designed and directed the METSIM study. Y.T. performed analysis in UK Biobank. M.V., P.N., L.-L.H., A.R., and N.P.C. performed validation experiments. M.K., L.Z.A., R.J.W.M., M.H., and K. Grove provided scientific feedback. J.Y., M.V., P.N., L.J.G., and M.K. wrote the manuscript.

DECLARATION OF INTERESTS

K. Grove is an employee of Novo Nordisk.

Received: February 4, 2022

Revised: June 29, 2022

Accepted: September 9, 2022

Published: October 4, 2022

REFERENCES

- Aibar, S., González-Blas, C.B., Moerman, T., Huynh-Thu, V.A., Imrichova, H., Hulselmans, G., Rambow, F., Marine, J.-C., Geurts, P., Aerts, J., et al. (2017). SCENIC: single-cell regulatory network inference and clustering. *Nat. Methods* **14**, 1083–1086.
- Amezquita, R.A., Lun, A.T.L., Becht, E., Carey, V.J., Carpp, L.N., Geistlinger, L., Marini, F., Rue-Albrecht, K., Risso, D., Sonesson, C., et al. (2020). Orchestrating single-cell analysis with Bioconductor. *Nat. Methods* **17**, 137–145.
- Ancel, S., Mashinchian, O., and Feige, J.N. (2019). Adipogenic progenitors keep muscle stem cells young. *Aging* **11**, 7331–7333.
- Aran, D., Looney, A.P., Liu, L., Wu, E., Fong, V., Hsu, A., Chak, S., Naikawadi, R.P., Woiters, P.J., Abate, A.R., et al. (2019). Reference-based analysis of lung single-cell sequencing reveals a transitional profibrotic macrophage. *Nat. Immunol.* **20**, 163–172.
- Bray, N.L., Pimentel, H., Melsted, P., and Pachter, L. (2016). Erratum: Near-optimal probabilistic RNA-seq quantification. *Nat. Biotechnol.* **34**, 888.
- Bycroft, C., Freeman, C., Petkova, D., Band, G., Elliott, L.T., Sharp, K., Motyer, A., Vukcevic, D., Delaneau, O., O'Connell, J., et al. (2018). The UK Biobank resource with deep phenotyping and genomic data. *Nature* **562**, 203–209.
- Camps, J., Breuls, N., Sifrim, A., Giarratana, N., Corvelyn, M., Danti, L., Grosemans, H., Vanuytven, S., Thiry, I., Belicchi, M., et al. (2020). Interstitial cell remodeling promotes aberrant adipogenesis in dystrophic muscles. *Cell Rep.* **31**, 107597.
- Chapman, M.A., Mukund, K., Subramaniam, S., Brenner, D., and Lieber, R.L. (2017). Three distinct cell populations express extracellular matrix proteins and increase in number during skeletal muscle fibrosis. *Am. J. Physiol. Cell Physiol.* **312**, C131–C143.
- Claussnitzer, M., Dankel, S.N., Kim, K.-H., Quon, G., Meuleman, W., Haugen, C., Glunk, V., Sousa, I.S., Beaudry, J.L., Puviindran, V., et al. (2015). FTO obesity variant circuitry and adipocyte browning in humans. *N. Engl. J. Med.* **373**, 895–907.
- Davey, J.R., Watt, K.I., Parker, B.L., Chaudhuri, R., Ryall, J.G., Cunningham, L., Qian, H., Sartorelli, V., Sandri, M., Chamberlain, J., et al. (2016). Integrated expression analysis of muscle hypertrophy identifies Asb2 as a negative regulator of muscle mass. *JCI Insight* **1**, e85477. <https://doi.org/10.1172/jci.insight.85477>.

- Dobin, A., Davis, C.A., Schlesinger, F., Drenkow, J., Zaleski, C., Jha, S., Batut, P., Chaisson, M., and Gingeras, T.R. (2013). STAR: ultrafast universal RNA-seq aligner. *Bioinformatics* 29, 15–21.
- Dong, H., Sun, W., Shen, Y., Baláz, M., Balázová, L., Ding, L., Löffler, M., Hamilton, B., Klötting, N., Blüher, M., et al. (2022). Identification of a regulatory pathway inhibiting adipogenesis via RSPO2. *Nat. Metab.* 4, 90–105.
- Dos Santos, M., Backer, S., Saintpierre, B., Izac, B., Andrieu, M., Letourneur, F., Relaix, F., Sotiropoulos, A., and Maire, P. (2020). Single-nucleus RNA-seq and FISH identify coordinated transcriptional activity in mammalian myofibers. *Nat. Commun.* 11, 5102.
- Efremova, M., Vento-Tormo, M., Teichmann, S.A., and Vento-Tormo, R. (2020). CellPhoneDB: inferring cell–cell communication from combined expression of multi-subunit ligand–receptor complexes. *Nat. Protoc.* 15, 1484–1506.
- Farmer, S.R. (2006). Transcriptional control of adipocyte formation. *Cell Metab.* 4, 263–273.
- Farr, L., Ghosh, S., and Moonah, S. (2020). Role of MIF cytokine/CD74 receptor pathway in protecting against injury and promoting repair. *Front. Immunol.* 11, 1273.
- Figueiredo, C.R., Azevedo, R.A., Mousdell, S., Resende-Lara, P.T., Ireland, L., Santos, A., Girola, N., Cunha, R.L.O.R., Schmid, M.C., Polonelli, L., et al. (2018). Blockade of MIF-CD74 signalling on macrophages and dendritic cells restores the antitumour immune response against metastatic melanoma. *Front. Immunol.* 9, 1132.
- Forcina, L., Miano, C., Scicchitano, B.M., Rizzuto, E., Berardinelli, M.G., De Benedetti, F., Pelosi, L., and Musarò, A. (2019). Increased circulating levels of interleukin-6 affect the redox balance in skeletal muscle. *Oxid. Med. Cell. Longev.* 2019, 3018584.
- Frankish, A., Diekhans, M., Ferreira, A.-M., Johnson, R., Jungreis, I., Loveland, J., Mudge, J.M., Sisu, C., Wright, J., Armstrong, J., et al. (2019). GENCODE reference annotation for the human and mouse genomes. *Nucleic Acids Res.* 47, D766–D773.
- Ghaben, A.L., and Scherer, P.E. (2019). Adipogenesis and metabolic health. *Nat. Rev. Mol. Cell Biol.* 20, 242–258.
- Giordani, L., He, G.J., Negroni, E., Sakai, H., Law, J.Y.C., Siu, M.M., Wan, R., Corneau, A., Tajbakhsh, S., Cheung, T.H., and Le Grand, F. (2019). High-dimensional single-cell cartography reveals novel skeletal muscle-resident cell populations. *Mol. Cell* 74, 609–621.e6.
- Giuliani, G., Rosina, M., and Reggio, A. (2021). Signaling pathways regulating the fate of fibro/adipogenic progenitors (FAPs) in skeletal muscle regeneration and disease. *FEBS J.* <https://doi.org/10.1111/febs.16080>.
- Gonzalez-Gil, A.M., and Elizondo-Montemayor, L. (2020). The role of exercise in the interplay between myokines, hepatokines, osteokines, adipokines, and modulation of inflammation for energy substrate redistribution and fat mass loss: a review. *Nutrients* 12, 1899. <https://doi.org/10.3390/nu12061899>.
- Gu, Z., Eils, R., and Schlesner, M. (2016). Complex heatmaps reveal patterns and correlations in multidimensional genomic data. *Bioinformatics* 32, 2847–2849.
- Gulati, G.S., Sikandar, S.S., Wesche, D.J., Manjunath, A., Bharadwaj, A., Berger, M.J., Ilagan, F., Kuo, A.H., Hsieh, R.W., Cai, S., et al. (2020). Single-cell transcriptional diversity is a hallmark of developmental potential. *Science* 367, 405–411.
- Gustavsen, J.A., Pai, S., Isserlin, R., Demchak, B., and Pico, A.R. (2019). RCy3: network biology using Cytoscape from within R. *F1000Res.* 8, 1774.
- Hafemeister, C., and Satija, R. (2019). Normalization and variance stabilization of single-cell RNA-seq data using regularized negative binomial regression. *Genome Biol.* 20, 296.
- Hahsler, M., Piekenbrock, M., and Doran, D. (2019). dbscan: fast density-based clustering with R. *J. Stat. Softw.* 91, 1–30.
- Henriques, F., Bedard, A.H., Guilherme, A., Kelly, M., Chi, J., Zhang, P., Lifshitz, L.M., Bellvé, K., Rowland, L.A., Yenilmez, B., et al. (2020). Single-cell RNA profiling reveals adipocyte to macrophage signaling sufficient to enhance thermogenesis. *Cell Rep.* 32, 107998. <https://doi.org/10.1016/j.celrep.2020.107998>.
- Hepler, C., Shan, B., Zhang, Q., Henry, G.H., Shao, M., Vishvanath, L., Ghaben, A.L., Mobley, A.B., Strand, D., Hon, G.C., and Gupta, R.K. (2018). Identification of functionally distinct fibro-inflammatory and adipogenic stromal subpopulations in visceral adipose tissue of adult mice. *eLife* 7, e39636.
- Ignatiadis, N., Klaus, B., Zaugg, J.B., and Huber, W. (2016). Data-driven hypothesis weighting increases detection power in genome-scale multiple testing. *Nat. Methods* 13, 577–580.
- Jia, G., and Sowers, J.R. (2019). Increased fibro-adipogenic progenitors and intramyocellular lipid accumulation in obesity-related skeletal muscle dysfunction. *Diabetes* 68, 18–20.
- Joe, A.W.B., Yi, L., Natarajan, A., Le Grand, F., So, L., Wang, J., Rudnicki, M.A., and Rossi, F.M.V. (2010). Muscle injury activates resident fibro/adipogenic progenitors that facilitate myogenesis. *Nat. Cell Biol.* 12, 153–163.
- Joffin, N., Paschoal, V.A., Gliniak, C.M., Crewe, C., Elnwasany, A., Szeweda, L.I., Zhang, Q., Hepler, C., Kusinski, C.M., Gordillo, R., et al. (2021). Mitochondrial metabolism is a key regulator of the fibro-inflammatory and adipogenic stromal subpopulations in white adipose tissue. *Cell Stem Cell* 28, 702–717.e8.
- Kalucka, J., de Rooij, L.P.M.H., Goveia, J., Rohlenova, K., Dumas, S.J., Meta, E., Concinha, N.V., Taverna, F., Teuwen, L.-A., Veys, K., et al. (2020). Single-cell transcriptome atlas of murine endothelial cells. *Cell* 180, 764–779.e20.
- Kim, Y.I., Lee, F.N., Choi, W.S., Lee, S., and Youn, J.H. (2006). Insulin regulation of skeletal muscle PDK4 mRNA expression is impaired in acute insulin-resistant states. *Diabetes* 55, 2311–2317.
- Kim, B.-S., Pallua, N., Bernhagen, J., and Bucala, R. (2015). The macrophage migration inhibitory factor protein superfamily in obesity and wound repair. *Exp. Mol. Med.* 47, e161.
- Kirwan, J.P., Sacks, J., and Nieuwoudt, S. (2017). The essential role of exercise in the management of type 2 diabetes. *Cleve. Clin. J. Med.* 84, S15–S21.
- Kobak, D., and Berens, P. (2019). The art of using t-SNE for single-cell transcriptomics. *Nat. Commun.* 10, 5416.
- Laakso, M., Kuusisto, J., Stančáková, A., Kuulasmaa, T., Pajukanta, P., Lusa, A.J., Collins, F.S., Mohlke, K.L., and Boehnke, M. (2017). The Metabolic Syndrome in Men study: a resource for studies of metabolic and cardiovascular diseases. *J. Lipid Res.* 58, 481–493.
- Lauritzen, H.P.M.M., Brandauer, J., Schjerling, P., Koh, H.-J., Treebak, J.T., Hirshman, M.F., Galbo, H., and Goodyear, L.J. (2013). Contraction and AICAR stimulate IL-6 vesicle depletion from skeletal muscle fibers in vivo. *Diabetes* 62, 3081–3092.
- Leal, L.G., Lopes, M.A., and Batista, M.L., Jr. (2018). Physical exercise-induced myokines and muscle-adipose tissue crosstalk: a review of current knowledge and the implications for health and metabolic diseases. *Front. Physiol.* 9, 1307.
- Lee, B.-C., Kim, H.-S., Shin, T.-H., Kang, I., Lee, J.Y., Kim, J.-J., Kang, H.K., Seo, Y., Lee, S., Yu, K.-R., et al. (2016). PGE2 maintains self-renewal of human adult stem cells via EP2-mediated autocrine signaling and its production is regulated by cell-to-cell contact. *Sci. Rep.* 6, 26298. <https://doi.org/10.1038/srep26298>.
- Li, C., Liu, B., Kang, B., Liu, Z., Liu, Y., Chen, C., Ren, X., and Zhang, Z. (2020a). SciBet as a portable and fast single cell type identifier. *Nat. Commun.* 11, 1818.
- Li, Y., Yun, K., and Mu, R. (2020b). A review on the biology and properties of adipose tissue macrophages involved in adipose tissue physiological and pathophysiological processes. *Lipids Health Dis.* 19, 164.
- Love, M.I., Huber, W., and Anders, S. (2014). Moderated estimation of fold change and dispersion for RNA-seq data with DESeq2. *Genome Biol.* 15, 550.
- Marcelin, G., Ferreira, A., Liu, Y., Atlan, M., Aron-Wisniewsky, J., Pelloux, V., Botbol, Y., Ambrosini, M., Fradet, M., Rouault, C., et al. (2017). A PDGFR α -mediated switch toward CD9^{high} adipocyte progenitors controls obesity-induced adipose tissue fibrosis. *Cell Metab.* 25, 673–685.
- Matsuo, F.S., Cavalcanti de Araújo, P.H., Mota, R.F., Carvalho, A.J.R., Santos de Queiroz, M., Baldo de Almeida, B., Ferreira, K.C.d.O.S., Metzner, R.J.M., Ferrari, G.D., Alberici, L.C., and Osako, M.K. (2020). RANKL induces beige adipocyte differentiation in preadipocytes. *Am. J. Physiol. Endocrinol. Metab.* 318, E866–E877.

- McGinnis, C.S., Murrow, L.M., and Gartner, Z.J. (2019). DoubletFinder: doublet detection in single-cell RNA sequencing data using artificial nearest neighbors. *Cell Syst.* **8**, 329–337.e4.
- McInnes, G., Tanigawa, Y., DeBoever, C., Lavertu, A., Olivieri, J.E., Aguirre, M., and Rivas, M.A. (2019). Global Biobank Engine: enabling genotype-phenotype browsing for biobank summary statistics. *Bioinformatics* **35**, 2495–2497.
- McQuin, C., Goodman, A., Chernyshev, V., Kametsky, L., Cimini, B.A., Karhohs, K.W., Doan, M., Ding, L., Rafelski, S.M., Thirstrup, D., et al. (2018). CellProfiler 3.0: next-generation image processing for biology. *PLoS Biol.* **16**, e2005970.
- Merrick, D., Sakers, A., Irgebay, Z., Okada, C., Calvert, C., Morley, M.P., Percec, I., and Seale, P. (2019). Identification of a mesenchymal progenitor cell hierarchy in adipose tissue. *Science* **364**, eaav2501. <https://doi.org/10.1126/science.aav2501>.
- Moon, H.Y., Song, P., Choi, C.S., Ryu, S.H., and Suh, P.-G. (2013). Involvement of exercise-induced macrophage migration inhibitory factor in the prevention of fatty liver disease. *J. Endocrinol.* **278**, 339–348.
- Newman, A.M., Liu, C.L., Green, M.R., Gentles, A.J., Feng, W., Xu, Y., Hoang, C.D., Diehn, M., and Alizadeh, A.A. (2015). Robust enumeration of cell subsets from tissue expression profiles. *Nat. Methods* **12**, 453–457.
- Newman, A.M., Steen, C.B., Liu, C.L., Gentles, A.J., Chaudhuri, A.A., Scherer, F., Khodadoust, M.S., Esfahani, M.S., Luca, B.A., Steiner, D., et al. (2019). Determining cell type abundance and expression from bulk tissues with digital cytometry. *Nat. Biotechnol.* **37**, 773–782.
- Nigro, P., Middelbeek, R.J.W., Alves, C.R.R., Rovira-Llopis, S., Ramachandran, K., Rowland, L.A., Møller, A.B., Takahashi, H., Alves-Wagner, A.B., Vamvini, M., et al. (2021). Exercise training promotes sex-specific adaptations in mouse inguinal white adipose tissue. *Diabetes* **70**, 1250–1264. <https://doi.org/10.2337/db20-0790>.
- Omatsu, Y., Seike, M., Sugiyama, T., Kume, T., and Nagasawa, T. (2014). Foxc1 is a critical regulator of haematopoietic stem/progenitor cell niche formation. *Nature* **508**, 536–540.
- Ongen, H., Buil, A., Brown, A.A., Dermitzakis, E.T., and Delaneau, O. (2016). Fast and efficient QTL mapper for thousands of molecular phenotypes. *Bioinformatics* **32**, 1479–1485.
- Opreescu, S.N., Yue, F., Qiu, J., Brito, L.F., and Kuang, S. (2020). Temporal dynamics and heterogeneity of cell populations during skeletal muscle regeneration. *iScience* **23**, 100993.
- Patro, R., Duggal, G., Love, M.I., Irizarry, R.A., and Kingsford, C. (2017). Salmon provides fast and bias-aware quantification of transcript expression. *Nat. Methods* **14**, 417–419.
- Qiu, X., Mao, Q., Tang, Y., Wang, L., Chawla, R., Pliner, H.A., and Trapnell, C. (2017). Reversed graph embedding resolves complex single-cell trajectories. *Nat. Methods* **14**, 979–982.
- Rajbhandari, P., Arneson, D., Hart, S.K., Ahn, I.S., Diamante, G., Santos, L.C., Zaghari, N., Feng, A.-C., Thomas, B.J., Vergnes, L., et al. (2019). Single cell analysis reveals immune cell–adipocyte crosstalk regulating the transcription of thermogenic adipocytes. *eLife* **8**, e49501.
- Ramirez, A.K., Dankel, S.N., Rastegarpanah, B., Cai, W., Xue, R., Crovella, M., Tseng, Y.-H., Kahn, C.R., and Kasif, S. (2020). Single-cell transcriptional networks in differentiating preadipocytes suggest drivers associated with tissue heterogeneity. *Nat. Commun.* **11**, 2117.
- Reggio, A., Rosina, M., Palma, A., Cerquone Perpetuini, A., Petrilli, L.L., Gargioli, C., Fuoco, C., Micarelli, E., Giuliani, G., Cerretani, M., et al. (2020). Adipogenesis of skeletal muscle fibro/adipogenic progenitors is affected by the WNT5a/GSK3/β-catenin axis. *Cell Death Differ.* **27**, 2921–2941.
- Robinson, M.D., McCarthy, D.J., and Smyth, G.K. (2010). edgeR: a Bioconductor package for differential expression analysis of digital gene expression data. *Bioinformatics* **26**, 139–140.
- Rubenstein, A.B., Smith, G.R., Raue, U., Begue, G., Minchev, K., Ruf-Zamojski, F., Nair, V.D., Wang, X., Zhou, L., Zaslavsky, E., et al. (2020). Single-cell transcriptional profiles in human skeletal muscle. *Sci. Rep.* **10**, 229.
- Sakurai, T., Ogasawara, J., Kizaki, T., Sato, S., Ishibashi, Y., Takahashi, M., Kobayashi, O., Oh-Ishi, S., Nagasawa, J., Takahashi, K., et al. (2013). The effects of exercise training on obesity-induced dysregulated expression of adipokines in white adipose tissue. *Int. J. Endocrinol.* **2013**, 801743.
- Sanford, J.A., Nogiec, C.D., Lindholm, M.E., Adkins, J.N., Amar, D., Dasari, S., Drugan, J.K., Fernández, F.M., Radom-Aizik, S., Schenk, S., et al. (2020). Molecular Transducers of Physical Activity Consortium (MoTrPAC): mapping the dynamic responses to exercise. *Cell* **181**, 1464–1474.
- Sárvári, A.K., Van Hauwaert, E.L., Markussen, L.K., Gammelmarm, E., Marcher, A.-B., Ebbesen, M.F., Nielsen, R., Brewer, J.R., Madsen, J.G.S., and Mandrup, S. (2021). Plasticity of epididymal adipose tissue in response to diet-induced obesity at single-nucleus resolution. *Cell Metab.* **33**, 437–453.e5.
- Schwalie, P.C., Dong, H., Zachara, M., Russeil, J., Alpern, D., Akkiche, N., Caprara, C., Sun, W., Schlaudraff, K.-U., Soldati, G., et al. (2018). A stromal cell population that inhibits adipogenesis in mammalian fat depots. *Nature* **559**, 103–108.
- Shannon, P., Markiel, A., Ozier, O., Baliga, N.S., Wang, J.T., Ramage, D., Amin, N., Schwikowski, B., and Ideker, T. (2003). Cytoscape: a software environment for integrated models of biomolecular interaction networks. *Genome Res.* **13**, 2498–2504.
- Shao, M., Hepler, C., Zhang, Q., Shan, B., Vishvanath, L., Henry, G.H., Zhao, S., An, Y.A., Wu, Y., Strand, D.W., and Gupta, R.K. (2021). Pathologic HIF1α signaling drives adipose progenitor dysfunction in obesity. *Cell Stem Cell* **28**, 685–701.e7.
- Sinnott-Armstrong, N., Tanigawa, Y., Amar, D., Mars, N., Benner, C., Aguirre, M., Venkataraman, G.R., Wainberg, M., Ollila, H.M., Kiiskinen, T., et al. (2021). Genetics of 35 blood and urine biomarkers in the UK Biobank. *Nat. Genet.* **53**, 185–194.
- Soliman, H., Paylor, B., Scott, R.W., Lemos, D.R., Chang, C., Arostegui, M., Low, M., Lee, C., Fiore, D., Braghetta, P., et al. (2020). Pathogenic potential of Hic1-expressing cardiac stromal progenitors. *Cell Stem Cell* **26**, 459–461.
- Son, S.S., Hwang, S., Park, J.H., Ko, Y., Yun, S.-I., Lee, J.-H., Son, B., Kim, T.R., Park, H.-O., and Lee, E.Y. (2021). In vivo silencing of amphiregulin by a novel effective self-assembled-micelle inhibitory RNA ameliorates renal fibrosis via inhibition of EGFR signals. *Sci. Rep.* **11**, 2191.
- Soneson, C., Love, M.I., and Robinson, M.D. (2015). Differential analyses for RNA-seq: transcript-level estimates improve gene-level inferences. *F1000Res.* **4**, 1521.
- Spallanzani, R.G., Zemmour, D., Xiao, T., Jayewickreme, T., Li, C., Bryce, P.J., Benoist, C., and Mathis, D. (2019). Distinct immunocyte-promoting and adipocyte-generating stromal components coordinate adipose tissue immune and metabolic tenors. *Sci. Immunol.* **4**, eaaw3658. <https://doi.org/10.1126/sciimmunol.aaw3658>.
- Stanford, K.I., Middelbeek, R.J.W., and Goodyear, L.J. (2015). Exercise effects on white adipose tissue: being and metabolic adaptations. *Diabetes* **64**, 2361–2368. <https://doi.org/10.2337/db15-0227>.
- Stenkula, K.G., and Erlanson-Albertsson, C. (2018). Adipose cell size: importance in health and disease. *Am. J. Physiol. Regul. Integr. Comp. Physiol.* **315**, R284–R295.
- Stephens, M. (2017). False discovery rates: a new deal. *Biostatistics* **18**, 275–294.
- Sudlow, C., Gallacher, J., Allen, N., Beral, V., Burton, P., Danesh, J., Downey, P., Elliott, P., Green, J., Landray, M., et al. (2015). UK biobank: an open access resource for identifying the causes of a wide range of complex diseases of middle and old age. *PLoS Med.* **12**, e1001779.
- Sue, N., Jack, B.H.A., Eaton, S.A., Pearson, R.C.M., Funnell, A.P.W., Turner, J., Czolij, R., Denyer, G., Bao, S., Molero-Navajas, J.C., et al. (2008). Targeted disruption of the basic Krüppel-like factor gene (Klf3) reveals a role in adipogenesis. *Mol. Cell Biol.* **28**, 3967–3978.
- Suzuki, C., Ushijima, K., Ando, H., Kitamura, H., Horiguchi, M., Akita, T., Yamashita, C., and Fujimura, A. (2019). Induction of Dbp by a histone deacetylase inhibitor is involved in amelioration of insulin sensitivity via adipocyte differentiation in ob/ob mice. *Chronobiol. Int.* **36**, 955–968.
- Tabula Muris Consortium; Overall coordination; Logistical coordination; Organ collection and processing; Library preparation and sequencing; Computational data analysis; Cell type annotation; Writing group;

Supplemental text writing group, and Principal investigators (2018). Single-cell transcriptomics of 20 mouse organs creates a Tabula Muris. *Nature* 562, 367–372.

Takahashi, H., Alves, C.R.R., Stanford, K.I., Middelbeek, R.J.W., Nigro, P., Ryan, R.E., Xue, R., Sakaguchi, M., Lynes, M.D., So, K., et al. (2019). TGF- β 2 is an exercise-induced adipokine that regulates glucose and fatty acid metabolism. *Nat. Metab.* 1, 291–303. <https://doi.org/10.1038/s42255-018-0030-7>.

Tucci, M., Quatraro, C., Dammacco, F., and Silvestris, F. (2007). Increased IL-18 production by dendritic cells in active inflammatory myopathies. *Ann. N. Y. Acad. Sci.* 1107, 184–192. <https://doi.org/10.1196/annals.1381.020>.

Ushijima, K., Suzuki, C., Kitamura, H., Shimada, K., Kawata, H., Tanaka, A., Horie, H., Hosoya, Y., Imai, Y., Yamashita, C., and Fujimura, A. (2020). Expression of clock gene *Dbp* in omental and mesenteric adipose tissue in patients with type 2 diabetes. *BMJ Open Diabetes Res. Care* 8, e001465. <https://doi.org/10.1136/bmjdr-2020-001465>.

Venkataraman, G.R., DeBoever, C., Tanigawa, Y., Aguirre, M., Ioannidis, A.G., Mostafavi, H., Spencer, C.C.A., Poterba, T., Bustamante, C.D., Daly, M.J., et al. (2021). Bayesian model comparison for rare variant association studies. *Am. J. Hum. Genet.* 108, 2354–2367.

Vijay, J., Gauthier, M.-F., Biswell, R.L., Louiselle, D.A., Johnston, J.J., Cheung, W.A., Belden, B., Pramatarova, A., Biertho, L., Gibson, M., et al. (2020). Single-cell analysis of human adipose tissue identifies depot- and disease-specific

cell types. *Nat. Metab.* 2, 97–109. <https://doi.org/10.1038/s42255-019-0152-6>.

Wang, F., Flanagan, J., Su, N., Wang, L.C., Bui, S., Nielson, A., Wu, X., Vo, H.T., Ma, X.J., and Luo, Y. (2012). RNAscope: a novel in situ RNA analysis platform for formalin-fixed, paraffin-embedded tissues. *J. Mol. Diagn.* 14, 22–29.

Wang, Y., Kuang, Z., Yu, X., Ruhn, K.A., Kubo, M., and Hooper, L.V. (2017). The intestinal microbiota regulates body composition through NFIL3 and the circadian clock. *Science* 357, 912–916.

Yoshitane, H., Asano, Y., Sagami, A., Sakai, S., Suzuki, Y., Okamura, H., Iwasaki, W., Ozaki, H., and Fukada, Y. (2019). Functional D-box sequences reset the circadian clock and drive mRNA rhythms. *Commun. Biol.* 2, 300.

Young, M.D., and Behjati, S. (2020). SoupX removes ambient RNA contamination from droplet-based single-cell RNA sequencing data. *GigaScience* 9, g1aa151. <https://doi.org/10.1093/gigascience/g1aa151>.

Zhou, Y., Zhou, B., Pache, L., Chang, M., Khodabakhshi, A.H., Tanaseichuk, O., Benner, C., and Chanda, S.K. (2019). Metascape provides a biologist-oriented resource for the analysis of systems-level datasets. *Nat. Commun.* 10, 1523.

Zvonic, S., Ptitsyn, A.A., Conrad, S.A., Scott, L.K., Floyd, Z.E., Kilroy, G., Wu, X., Goh, B.C., Mynatt, R.L., and Gimble, J.M. (2006). Characterization of peripheral circadian clocks in adipose tissues. *Diabetes* 55, 962–970.

STAR★METHODS

KEY RESOURCES TABLE

REAGENT or RESOURCE	SOURCE	IDENTIFIER
Antibodies		
anti-CD45	Biolegend	103133; RRID: AB_10899570
anti-CD34	Biolegend	128609; RRID: AB_10899570
anti-CD140a	Biolegend	135911; RRID: AB_10899570
anti-SCA1	Biolegend	122511; RRID: AB_10899570
anti-SCA1	Thermo Fisher Scientific	710952; RRID: AB_2609699
anti-PDGFR α	Origene	TA807645
anti-LAMA4	R&D Systems	AF3837; RRID: AB_2249744
Chemicals, peptides, and recombinant proteins		
Isoflurane	Piramal Healthcare	60307-120
Gill 3 Hematoxylin	Richard Allan Scientific	72604
Eosin Y	Richard Allan Scientific	71311
Cytox green	Invitrogen	S34860
Critical commercial assays		
Direct-zol RNA MiniPrep	Zymo Research	R2050
Advantage 2 Polymerase Mix	TaKaRa Bio	639201
Adipose tissue dissociation kit	Miltenyi Biotec	130-105-808
Skeletal muscle tissue dissociation kit	Miltenyi Biotec	130-098-305
Chromium Single Cell 3' RNA reagent kit v3	10X Genomics	1000075
Dead cell removal MS column	Miltenyi Biotec	130-042-201
Dead cell removal kit	Miltenyi Biotec	130-090-101
miRNeasy micro kit	Qiagen	217084
RNAscope LS Multiplex Reagent Kit	Advanced Cell Diagnostics	322800
Deposited data		
Mouse scWAT, vWAT and SkM exercise-obesity bulk RNA-seq data	This paper	GEO: GSE183239
Mouse scWAT, vWAT and SKM exercise-obesity single-cell RNA-seq data	This paper	GEO: GSE183288
Raw data	This paper	Data S1
Experimental models: Organisms/strains		
C57BL/6 N mice	Charles River Laboratories	N/A
Oligonucleotides		
See bulk mRNA sequencing section for oligos and primers	N/A	N/A
Pdgfra-F: AGAGTTACACGTTTGTGCTGTC; Pdgfra-R: GTCCCTCCACGGTACTCCT	Integrated DNA Technologies	N/A
Ly6a-F: AGGAGGCAGCAGTTATTGTGG; Ly6a-R: CGTTGACCTTAGTACCCAGGA	Integrated DNA Technologies	N/A
Dpt-F: TGGATGGGTGAATCTTAACCGC; Dpt-R: TCAGAGCCTTCTTCTTGCTA	Integrated DNA Technologies	N/A
Apoe-F: CTGACAGGATGCCTAGCCG; Apoe-R: CGCAGGTAATCCAGAAAGC	Integrated DNA Technologies	N/A
Mm-Ly6a-C3	Advanced Cell Diagnostics	427578-C3
Mm-Pdgfra-C4	Advanced Cell Diagnostics	480668-C4

(Continued on next page)

Continued

REAGENT or RESOURCE	SOURCE	IDENTIFIER
Software and algorithms		
CellProfiler 3.0	(McQuin et al., 2018)	http://cellprofiler.org
Salmon 0.14.2	(Patro et al., 2017)	https://salmon.readthedocs.io/en/latest/salmon.html
CIBERSORTx	(Newman et al., 2019)	https://cibersortx.stanford.edu/
Cell Ranger software v4.0.0	10X Genomics	https://support.10xgenomics.com/single-cell-gene-expression/software/pipelines/latest/what-is-cell-ranger
CellPhoneDB	(Efremova et al., 2020)	https://github.com/ventolab/CellphoneDB
Cytoscape	(Shannon et al., 2003)	https://cytoscape.org/
R 4.0.4	See quantification and statistical analysis section for R packages used	https://www.r-project.org/about.html
STAR v2.5.2b	(Dobin et al., 2013)	https://github.com/alexdobin/STAR
Kallisto	(Bray et al., 2016)	https://pachterlab.github.io/kallisto/about
FastQTL	(Ongen et al., 2016)	https://github.com/francois-a/fastqtl
Metascape	(Zhou et al., 2019)	https://metascape.org/gp/index.html#/main/step1
Prism v9	GraphPad Software	http://www.graphpad.com
Other		
10% kcal fat LabDiet	PharmaServ	9F5020
60% kcal fat LabDiet	PharmaServ	9F5020
24 cm running wheel	NalGene	N/A

RESOURCE AVAILABILITY

Lead contact

Further information and requests for resources and reagents should be directed to and will be fulfilled by the lead contact, Manolis Kellis (manoli@mit.edu).

Materials availability

This study did not generate new unique materials.

Data and code availability

- All raw and processed bulk mRNA-seq and scRNA-seq data have been uploaded in the GEO database (<https://www.ncbi.nlm.nih.gov/gds>) with the accession numbers GEO: GSE183239 and GSE183288 under SuperSeries GEO: GSE183290. We also provide an interactive data and analysis browser for all the data at <http://scmetab.mit.edu/>. Additional supplemental figures and tables were deposited in Zenodo: <https://doi.org/10.5281/zenodo.7011615>.
- Original codes for data analysis were deposited on Github at <https://github.com/KellisLab/scmetab>.
- All values used to generate the graphs of the paper can be found in the file [Data S1 – Source Data](#). Any additional information required to reanalyze the data reported in this paper is available from the lead contact upon request.

EXPERIMENTAL MODEL AND SUBJECT DETAILS

All experiments were conducted following NIH guidelines and protocols were approved by the Institutional Animal Care and Use Committee at Joslin Diabetes Center in Boston, MA. C57BL/6 N mice were purchased from the Charles River Laboratories and were housed in singular cages at room temperature (23°C) on a 12 h/12 h light/dark cycle (6a [ON]/6p [OFF]) in an AAALAC-approved animal facility at Joslin Diabetes Center. The mice were given *ad libitum* access to food and water and fed either a standard chow-diet (10% kcal fat; 9F5020-LabDiet, PharmaServ) or an HFD (60% kcal fat; 9F5020-LabDiet, PharmaServ). Any mouse that ran less than 3 km/day was excluded from analyses. Mice were anesthetized 24 h after the last bout of exercise and following a 6-h fast, using Isoflurane and heart puncture. We used 5% v/v Isoflurane (NDC 60307-120, Piramal Healthcare) which was administered with an EZ-150C anesthesia machine (E-Z Systems). Tissues were then rapidly dissected and processed or stored for analysis. All participants of the METSIM cohort provided informed consent and the study was approved by the ethics committee of the University of Eastern Finland. The genetic analysis in UK Biobank has been conducted using the UK Biobank Resource under Application Number 21942, “Integrated models of complex traits in the UK Biobank” (<https://www.ukbiobank.ac.uk/enable-your-research/approved->

research/integrated-models-of-complex-traits-in-the-uk-biobank). All participants of the UK Biobank provided written informed consent (more information is available at <https://www.ukbiobank.ac.uk/2018/02/gdpr/>).

METHOD DETAILS

Animals, exercise, and sample collection

We used 6-week-old male mice for this experiment. For the first 3 weeks, all mice were sedentary, and half of the mice were fed a chow standard diet (10% kcal fat; 9F5020-LabDiet, PharmaServ) and the other half a HFD (60% kcal fat; 9F5020-LabDiet, PharmaServ) *ad libitum*. HFD feeding was used as a robust model for the development of impaired glucose tolerance. At the start of week 4, mice were further divided into sedentary and training groups, resulting in four groups: sedentary chow-fed; exercise training chow-fed; sedentary HFD fed; and exercise training HFD fed. The mouse cohort consisted of 60 mice: 12 in each sedentary group (12 chow; 12 HFD) and 18 in each training group (18 standard diet; 18 HFD). Exercise training was done by housing mice in individual cages containing a running wheel. Mice had free access to the wheel at all times, and running distance was recorded daily. Sedentary mice were individually housed in standard cages. All mice had body weights measured every two days. After 21 days, mice underwent a glucose tolerance test (GTT) after a 12-h fast. Seven days later (day 28), the wheels of the trained mice were locked. Twenty-four hours later, following a 6-h fast, mice were anesthetized with 5% v/v Isoflurane (NDC 60307-120, Piramal Healthcare) using EZ-150C anesthesia machine (E-Z Systems) and blood was drawn by heart puncture. Perigonadal visceral (vWAT) and inguinal subcutaneous white adipose tissue (scWAT) and triceps muscle were rapidly dissected and were either snap frozen or processed fresh to generate cell suspension.

Bulk mRNA sequencing

For the whole-tissue RNAseq, also known as bulkRNAseq, we euthanized 5 mice per group and harvested inguinal and perigonadal WAT as well as triceps. These tissues were snap frozen in liquid nitrogen immediately after collection. Total RNA was extracted at the Goodyear lab using an RNA extraction kit (Direct-zol RNA MiniPrep, Zymo Research). 10 ng of total RNA quantified and quality assessed by Advanced Analytical Fragment Analyzer was used for library preparation on Tecan Evo150. 3' DGE-custom primers 3V6NEXT-bmc#1-12 were added to a final concentration of 1 μ M. (5'-/5Biosg/ACACTCTTCCCTACACGACGCTCTTCCGATCT [BC6]N10T30VN-3' where 5Biosg = 5' biotin, [BC6] = 6 bp barcode specific to each sample/well, N10 = Unique Molecular Identifiers, Integrated DNA technologies), to generate two subpools of 15 samples each. After addition of the oligonucleotides, Maxima H Minus RT was added per manufacturer's recommendations with Template-Switching oligo 5V6NEXT (10 μ M, [5V6NEXT: 5'-iCiGiCA CACTCTTCCCTACACGACGCrGrG-3' where iC: iso-dC, iG: iso-dG, rG: RNA G]) followed by incubation at 42°C for 90' and inactivation at 80°C for 10'. Following the template switching reaction, cDNA from 12 wells containing unique well identifiers were pooled together and cleaned using RNA Ampure beads at 1.0X. cDNA was eluted with 17 μ l of water followed by digestion with Exonuclease I at 37°C for 30 min, and inactivated at 80°C for 20 min.

Second strand synthesis and PCR amplification was done by adding the Advantage 2 Polymerase Mix (Clontech) and the SINGV6 primer (10 pmol, Integrated DNA Technologies 5'-/5Biosg/ACACTCTTCCCTACACGACGC-3') directly to the exonuclease reaction. Eight cycles of PCR were performed followed by clean up using regular SPRI beads at 0.6X, and eluted with 20 μ l of elution buffer (Qiagen). Successful amplification of cDNA was confirmed using the Fragment Analyzer.

Illumina libraries were then produced using standard Nextera tagmentation substituting P5NEXTPT5-bmc primer (25 μ M, Integrated DNA Technologies, 5'-AATGATACGGCACCACCGAGATCTACACTCTTCCCTACACGACGCTCTTCCG*A*T*C*T*-3' where * = phosphorothioate bonds) in place of the normal N500 primer. Final libraries were cleaned using SPRI beads at 0.7X and quantified using the Fragment Analyzer and qPCR before being loaded for sequencing using the HiSeq 2000 (Illumina, Inc) in 50 bp single-end mode at the BioMicro Center at MIT.

Single-cell RNA sequencing

Tissues from 2-3 mice were pooled to achieve $>1 \times 10^6$ analyzable cells (final sample size per group = 3-4). Fresh tissues were enzymatically digested and dissociated according to tissue dissociation kit protocols (adipose tissue Cat No 130-105-808, skeletal muscle Cat No 130-098-305 by Miltenyi) using the gentleMACS Dissociator (Miltenyi). Dissociated tissues were filtered, centrifuged, and the isolated cells were resuspended in 0.1% BSA in PBS and immediately processed for the generation of single-cell RNA (scRNA) libraries using the droplet-based RNA sequencing technology. Briefly, 5000-6000 cells were profiled per sample using the Chromium Single Cell 3' RNA reagent kit v3 according to the 10X Genomics protocol. The generated cDNA libraries were indexed, pooled, and sequenced in three batches using the NovaSeq 6000 S2 system and reagent kits (100 cycles; Illumina) at the BioMicro Center Core at MIT.

Histology

Representative samples of scWAT and vWAT were fixed with 3.7% formaldehyde for 24hrs and then stored in 70% ethanol at 4°C. Five-micrometer-thick tissue sections were stained with hematoxylin and eosin (Richard Allan Scientific) and relative adipocyte size was estimated at 20-fold magnification of 5 random fields using an inverted fluorescence microscope (IX51Olympus). CellProfiler 3.0 (<http://cellprofiler.org>) was used for the automatic measurement.

FACS-based cell isolation, RNA isolation and quantitative PCR

Single cell suspension passed through 40 μm (FisherBrand) and dead cell removal MS column (Miltenyi Biotec) were stained with anti-CD45 BV650 antibody (1:100, Biolegend), anti-CD34 PE antibody (1:100, Biolegend), anti-CD140 PE-Cy7 (1:100, Biolegend), anti-SCA1 BV421 (1:100, Biolegend) in PBS containing 0.1% BSA at 4°C for 30 min. After 3 times of washing, Cytox green (1:100, Invitrogen) was added as a dead cell marker. Live CD140⁺ SCA1⁺ and CD140⁺SCA1⁻ cells from CD45⁻CD34⁺ populations were sorted on Aria II (BD biosciences), and the RNA were isolated using Trizol in combination with miRNeasy kit (Qiagen). 15 μl of elution buffer was used to elute RNA, and we performed qRT-PCR using RNA to Ct kit on Quant Studio 7 (Thermo Scientific) to detect gene differentially expressed in CD140⁺SCA1⁺ and CD140⁺SCA1⁻.

RNAscope LS Multiplex Fluorescent ISH assay

RNA *in situ* hybridization experiments were performed using the RNAscope technology, which has been previously described (Wang et al., 2012). Paired double-Z oligonucleotide probes were designed against target RNA using custom software. The RNAscope LS Fluorescent Multiplex Kit and the probes targeting mouse *pdgfr* variant 1 and *ly6a* mRNA were from Advanced Cell Diagnostics (Newark CA). The RNAscope LS Fluorescent Multiplex Kit was used with standard pre-treatment conditions. FFPE mouse skeletal muscle tissue samples were incubated with Leica BOND Epitope Retrieval Solution 2 (ER2) at 95°C for 15 min. RNAscope 2.5 LS Protease III was used for 15 min at 40°C. Pre-treatment conditions were optimized for each sample and quality control for RNA integrity was completed using probes specific to the housekeeping genes *Polr2a*, *Ppib*, and *Ubc*. These probes are low, moderate, and high expressing genes, respectively. Negative control background staining was evaluated using a probe specific to the bacterial *dapB* gene. Fluorescent images were acquired using a 3D Histech Panoramic Scan Digital Slide Scanner microscope using a 40x objective.

Immunohistochemistry assay

The 5 μm gastrocnemius muscles sections were fixed with 3.7% formaldehyde for 24hrs, embedded in paraffin and submitted to antigen retrieval with a hot 1x sodium citrate buffer (10 mM sodium citrate, 0.05% Tween 20, pH6). Immunofluorescence was carried out using 15 $\mu\text{g}/\text{mL}$ anti-SCA1 (710952, ThermoFisher), 5 $\mu\text{g}/\text{mL}$ anti-PDGFR α (TA807645 S, Origene), and 15 $\mu\text{g}/\text{mL}$ anti-LAMA4 (AF3837-SP, R&D Systems). Primary antibodies were incubated overnight at 4°C. Secondary antibodies were anti-mouse Alexa 488, anti-rabbit Alexa 568, and anti-goat Alexa 647 at a 1:400 dilution. Secondary antibodies were incubated for 1 h at room temperature. The slides were mounted with Vectashield with DAPI to counterstain nuclei. Immunofluorescence images were obtained with a confocal laser scanning microscope (Zeiss LSM 710).

QUANTIFICATION AND STATISTICAL ANALYSIS

Analysis of bulk mRNA-seq data

Pre-processing and DE analysis

Six FASTQ files for each sample were concatenated for read de-duplication using unique molecular identifiers (UMIs). We then ran Salmon 0.14.2 (Patro et al., 2017) to quantify the number of unique reads for each transcript against Ensembl version 98 mouse transcripts. The transcript level information was summarized to the gene-level using R package tximport (Soneson et al., 2015). We then clustered all the samples across three tissues unbiasedly to observe potential batch effects and sample outliers. Next for each tissue, genes with a count greater than 10 in all the samples were retained, and differential gene expression analysis for our three comparisons was carried out using R package DESeq2 (Love et al., 2014). We used Independent Hypothesis Weighting (IHW; Ignatiadis et al., 2016) to adjust p values and adaptive shrinkage estimator (ashr; Stephens, 2017) to adjust fold changes from DESeq2 results. We called significant DEGs at an adjusted p value cutoff of 0.05 (Table S1).

Deconvolution

We performed deconvolution on bulk mRNA-seq data using CIBERSORTx (Newman et al., 2019) and in reference to two publicly available datasets (Dos Santos et al., 2020; Rajbhandari et al., 2019): one is a scRNA-seq data in scWAT and the other is a snRNA-seq data in skeletal muscle. We integrated and re-annotated the scWAT scRNA-seq dataset, and confirmed original cell type annotation for the skeletal muscle snRNA-seq dataset (figures on Zenodo). We ran CIBERSORTx using default parameters for all three analysis modules, including creating signature matrices using the two reference datasets, imputing cell fractions, and sample-level gene expression using our bulk data. We calculated expression changes for genes with imputed expression levels in the three comparisons using the Wilcoxon rank sum test.

scRNA-seq data analysis

Pre-processing, clustering and annotation

Gene count matrices for each single-cell sample were generated by aligning reads to the mm10 genome (refdata-gex-mm10-2020-A) using 10X Genomics Cell Ranger software v4.0.0. We profiled 317,754 cells across 42 libraries from 93 tissue samples (pooling tissues from 2-3 mice to obtain enough cells), capturing 6501 cells per library, 2025 genes per cell, and 45,421 reads per cell on average. We clustered pseudo-bulk profiles of individual single-cell samples to determine potential batch effects, and excluded one low-quality sample based on unbiased clustering results. Then for each sample, we removed ambient RNA contamination using SoupX (Young and Behjati, 2020) with a fixed contamination fraction of 20%. The 20% fixed threshold performed the best compared to no ambient RNA removal, automatic removal implemented in SoupX, 10 and 15% fixed thresholds, and threshold estimated using

hemoglobin genes, to reach a desirable de-contaminated visualization and keep the greatest number of cells. We then excluded low-quality cells using four QC metrics: (i) number of genes with non-zero expression fewer than 500; (ii) number of UMIs fewer than 200 or more than 6000; (iii) percentage of reads mapping to mitochondrial genes more than 10; and (iv) number of reads mapped to Mki67 more than 0. We removed potential cell doublets using DoubletFinder (McGinnis et al., 2019) with default parameters and 3.1% homotypic doublet proportion estimation based on statistics published by 10X Genomics. After stringent QC, we report expression levels for a total of 17,341 genes across 204,883 cells. Next we integrated all the 41 samples across three tissues together for an atlas, and samples belonging to a single tissue together for tissue-specific maps. Integration was done without any batch correction using Seurat v3 (Hafemeister and Satija, 2019). We used “sctransform” in Seurat for data normalization, performed principal component analysis (PCA) to obtain the first 50 PCs, used the 50 PCs to build community, and clustered the cells using both a graph-based clustering approach as implemented in Seurat v3 and a density-based clustering approach in R package dbSCAN (Hahsler et al., 2019). Visualization of the tissue- and atlas-level datasets was through non-linear dimensional reduction techniques such as tSNE and UMAP. We adjusted processing steps for tSNE in reference to this paper (Kobak and Berens, 2019). We then annotated cell clusters using SciBet (Li et al., 2020a), SingleR (Aran et al., 2019), and cell type-specific markers from *Tabula Muris* (Tabula Muris Consortium et al., 2018) and tissue-focused studies in the field (Giordani et al., 2019; Merrick et al., 2019; Opreescu et al., 2020; Ramirez et al., 2020). For unknown cell type subclusters like Sca1⁺ FAP, we identified cell type-specific markers using the “FindMarkers” function in Seurat with an expression cutoff of 25% in either of the two tested populations. We further subsetted each cell type and performed sub-clustering within the cell type to identify cell subtypes/states. We annotated identified cell subtypes/states referencing markers from the literature. We distinguished: (a) follicular vs. memory B-cells; (b) M1 vs. M2 macrophages; (c) T-cell subtypes including CD8 naive, CD8 cytotoxic, CD4 naive, CD4 memory, T regulatory (Treg), NKT, and naive (Cd27⁻) vs. memory (Cd27⁺) gamma-delta (Tgd); (d) dendritic cell (DC) subtypes conventional type 1, type 2, and monocyte-derived; (e) inflammatory vs. patrolling monocytes; (f) six tenocyte subtypes, including *Pdgfra* + tendon stem/progenitor cells (TSPCs), *pre_Dpp4+*, *Dpp4+*, *Col22a1+*, *Pappa2+*, and *Scx-*; (g) vascular smooth muscle cells (SMCs) vs. SMC precursors vs. pericytes; (h) endothelial subtypes (Kalucka et al., 2020) associated with large vessel vs. large artery vs. capillary vs. lymphatic vessel; (i) myelinating vs. non-myelinating glial (Schwann) cells; (j) three states of ASCs in WAT, including interstitial progenitor cells (IPCs, marked by *Dpp4+/Pi16+*), committed pre-adipocytes (CPs, marked by *Icam1+/Fabp4+*), and CD142⁺ cells (defined as CD142⁺/*Fmo2+* Dong et al., 2022; Merrick et al., 2019; Schwalie et al., 2018), and a fourth state specific to vWAT (*pre_CP*), lying between IPCs and CPs and expressing both *Dpp4* and *Icam1*; and (k) seven states of FAPs.

DE analysis

We performed cell-type- and cell-state-specific differential expression (DE) analysis on “pseudo-bulk” profiles, generated by summing counts together for all cells with the same combination of cell type/state and sample. This approach leverages the resolution offered by single-cell technologies to define cell types/states, and combines it with the statistical rigor of existing methods for DE analysis involving a small number of samples (Amezquita et al., 2020). The DE analysis was performed using quasi-likelihood (QL) methods from the edgeR package (Robinson et al., 2010). We removed cell type/state and sample combinations containing fewer than 10 cells. Cell-type/state-specific DE-Gs were determined using an FDR cutoff of 0.05 (Table S4).

Cellular communication

For within- and cross-tissue communication prediction, we exported gene-by-cell count matrices and cell type/state assignment for each cell as two input files for CellPhoneDB “statistical analysis” (Efremova et al., 2020). CellPhoneDB is a publicly available repository of curated receptors, ligands and their interactions with the advantage of taking subunit architecture into consideration. We then imported CellPhoneDB results into R, merged interactions identified in each sample, and compared rank and mean values for all the interacting partners of an interaction in our three defined comparisons (“obesity”, “training”, and “rescue”). Specifically for cross-tissue interactions, we forced ligands to be secretable and interactions to be non-integrin. We then derived log₂ fold changes using mean value, and calculated statistical significance on ranks using the Wilcoxon rank sum test implemented in base R. Interactions with a nominal p value of 0.1 were plotted using Rcy3 package (Gustavsen et al., 2019) and Cytoscape (Table S5).

Gene regulatory network and CytoTRACE

We inferred per-sample GRNs using SCENIC with GRNBoost implementation in Python (Aibar et al., 2017), and detected regulons with differential activities between intervention groups using the Wilcoxon rank sum test. We estimated differentiation stages of ASCs and FAPs using the script provided with the CytoTRACE framework (Gulati et al., 2020). CytoTRACE leverages a simple, yet robust, determinant of developmental potential—the number of detectably expressed genes per cell, or gene counts to predict the differentiation state of cells from single-cell RNA-seq data. All the QC steps and analysis performed on single-cell data were illustrated and summarized in a figure deposited to Zenodo.

METSIM and UK biobank analysis

METSIM RNA-seq

The METSIM cohort consists of 10,197 Finnish men with detailed metabolic phenotyping (Laakso et al., 2017). Among these, we analyzed 335 participants with RNA-seq data from subcutaneous adipose tissue biopsies. Reads were mapped using STAR v2.5.2b (Dobin et al., 2013) to the GRCh38 genome with Gencode (Frankish et al., 2019) v26 as a transcriptome annotation. Gene read counts were calculated using FeatureCounts. We performed transcriptome-wide differential expression for insulin, glucose, Homa-IR, C-reactive protein (CRP), free fatty acids (FFA), Matsuda index, BMI, and waist-hip ratio adjusted for BMI (WHRadjBMI). All phenotypes except WHRadjBMI were log-transformed to induce an approximate normal distribution. To improve

power, we included RIN, the first PC, and sequencing batch as covariates. Normalization factors for library size were calculated using Trimmed Mean of M-values (TMM). To perform DE, we used edgeR v3.22.5 (Robinson et al., 2010) with the quasi-likelihoods to fit the models and obtain p values. P-values were adjusted for multiple testing using FDR.

METSIM isoform QTL

To estimate isoform transcript abundance, we ran Kallisto (Bray et al., 2016) using Gencode v26 as a transcriptome reference. Isoform QTLs were detected with FastQTL (Ongen et al., 2016). Isoform transcripts per million (TPM) estimates from Kallisto were rank transformed to a standard normal distribution. FastQTL was run using RIN, batch, and the first 35 PCs as covariates. To determine the number of PCs, a QTL analysis was run on chromosome 21 with successively larger numbers of PCs as covariates. We selected 35 as this roughly maximized the number of isoform QTLs. We extracted nominal p values and corrected for multiple testing as follows. For each isoform, we corrected SNP-isoform p values using Benjamini-Hochberg. Then, we corrected the q-values for the number of isoforms tested using Bonferroni.

UK biobank

To assess the phenome-wide associations of the genetic variants in *DBP* and *CDKN1A* across anthropometric and metabolic traits in human, we investigated GWAS summary statistics across 8 variants in the two candidate genes and 108 traits in UK Biobank. Briefly, we focused on meta-analyzed GWAS summary statistics on directly genotyped arrays (Bycroft et al., 2018) across a total of 451,354 individuals consisting of white British (n = 337,129), non-British white (n = 44,632), African (n = 6,497), South Asian (n = 7,831), East Asian (n = 1,704), semi-related (n = 44,632), and admixed (n = 28,656) individuals, defined from a combination of genotype PCs and self-reported ancestry as described elsewhere (Sinnott-Armstrong et al., 2021; Venkataraman et al., 2021). The association summary statistics was visualized with R 'ggforestplot' package (<https://nightingalehealth.github.io/ggforestplot/index.html>) and is available as a part of Global Biobank Engine (McInnes et al., 2019).

Other computational analyses and data processing remarks

Enrichment analysis was performed using the web server Metascape with default parameters (Zhou et al., 2019). All the heatmaps were generated using R package ComplexHeatmap (Gu et al., 2016). All computational analyses were performed using R version 3.4.0. All Wilcoxon rank sum tests were unpaired and two-sided. All two-way ANOVA followed by Tukey multiple comparison tests were generated in GraphPad Prism v9. All boxplots were generated and displayed in R, using the `geom_boxplot()` function with default parameters. The median value is indicated with a black line, and a colored box (hinges) is drawn between the 1st and 3rd quartiles (interquartile range, IQR). The whiskers correspond to no further than 1.5 x IQR from the hinge and outliers are omitted. All bar plots for phenotype analysis were generated and displayed in Prism, which display mean values as centers and the standard deviation as error bars. All included microscopy images are representative.

Supplemental information

Single-cell dissection of the obesity-exercise

axis in adipose-muscle tissues

implies a critical role for mesenchymal stem cells

Jiekun Yang, Maria Vamvini, Pasquale Nigro, Li-Lun Ho, Kyriakitsa Galani, Marcus Alvarez, Yosuke Tanigawa, Ashley Renfro, Nicholas P. Carbone, Markku Laakso, Leandro Z. Agudelo, Päivi Pajukanta, Michael F. Hirshman, Roeland J.W. Middelbeek, Kevin Grove, Laurie J. Goodyear, and Manolis Kellis

Figure S1

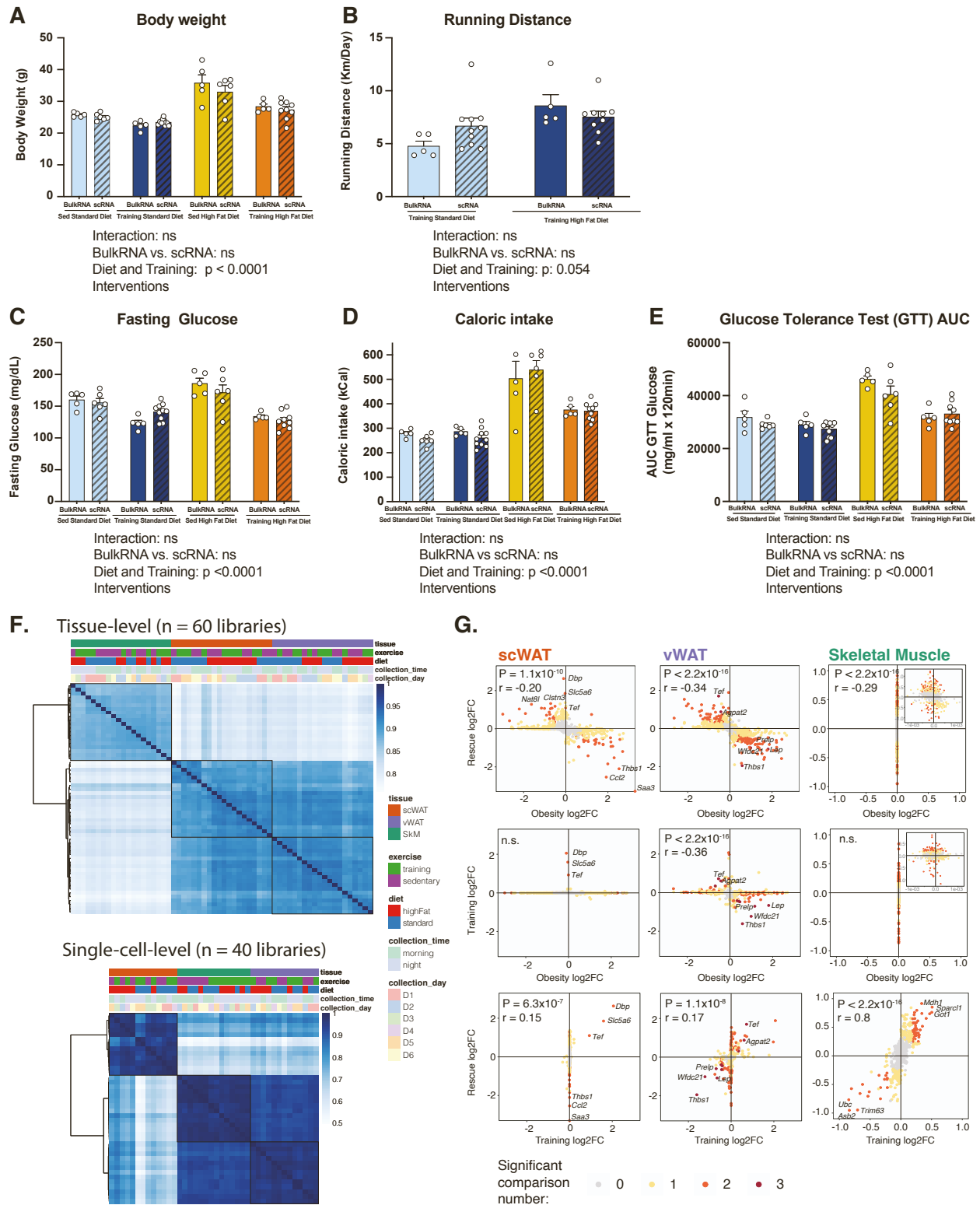


Figure S1. Phenotypic responses of the bulk and single-cell mouse cohorts, sample clustering, and cross-phenotypic-comparison tissue-level transcriptomic change correlation (related to Figures 1 and 2). (A-E) Body weight (A), running distance (B), fasting glucose (C), caloric intake (D), and glucose tolerance test (GTT) result (E) for mice used in bulk and single-cell analysis across the four intervention groups. There is no statistically significant difference between the two cohorts for the metrics shown. Statistical comparisons were performed using 2-way ANOVA, and data are represented as mean \pm SEM (A-E). (F) Unbiased clustering of tissue- and single-cell-level samples with variables that may introduce batch effects shown on the top. The variables include tissue type, exercise group, diet group, and tissue collection time and day. Clustering results of the bulk data were mainly driven by the parenchymal cell types in each tissue. Clustering results of the single-cell data were mainly driven by abundance of the shared (e.g., more vascular cell types in vWAT and SkM) and distinct (e.g., lymph node-resident cells in scWAT) cell types captured in our single-cell assay. (G) Global transcriptomic change correlation across “obesity”, “training”, and “rescue” comparisons in scWAT (left), vWAT (middle), and skeletal muscle. The P and r values in panel G were obtained from correlation tests. ns, not significant; AUC, area under curve; FC, fold change. Other abbreviations used in this figure appear in the Methods.

Figure S2

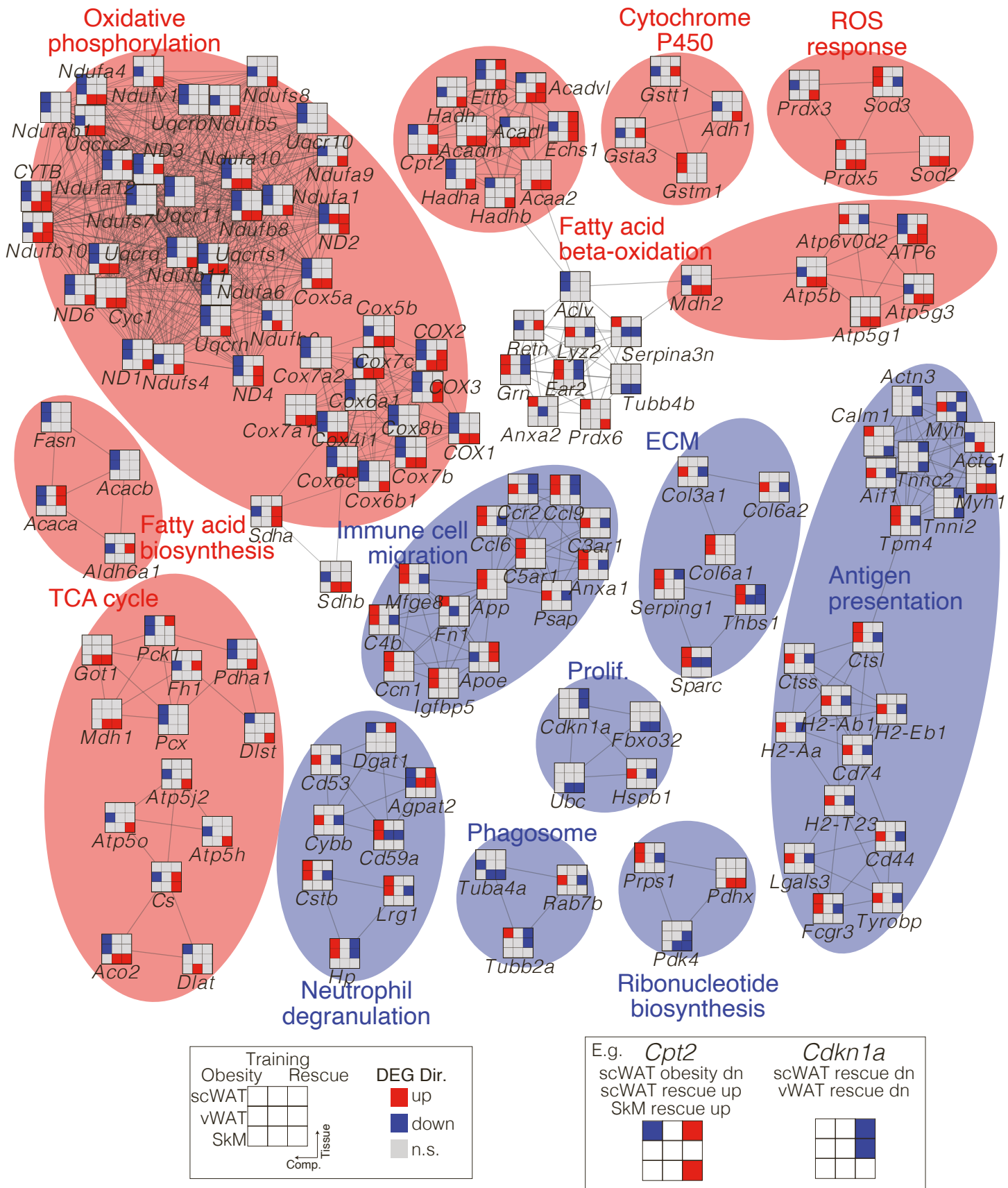


Figure S2. Tissue-level protein-protein interaction network (related to Figure 2). Gene networks across selected DEGs from the three tissues that encode interacting proteins, clustered by protein-protein interactions with each cluster named by the most significantly enriched pathway. The 3-by-3 grid of each node (gene) is coloured by DEG direction in the three tissues (row) and comparisons (column). The cluster is coloured by DEG direction with exercise training. ECM, extracellular matrix; Prolif, proliferation; ROS, reactive oxygen species.

Figure S3

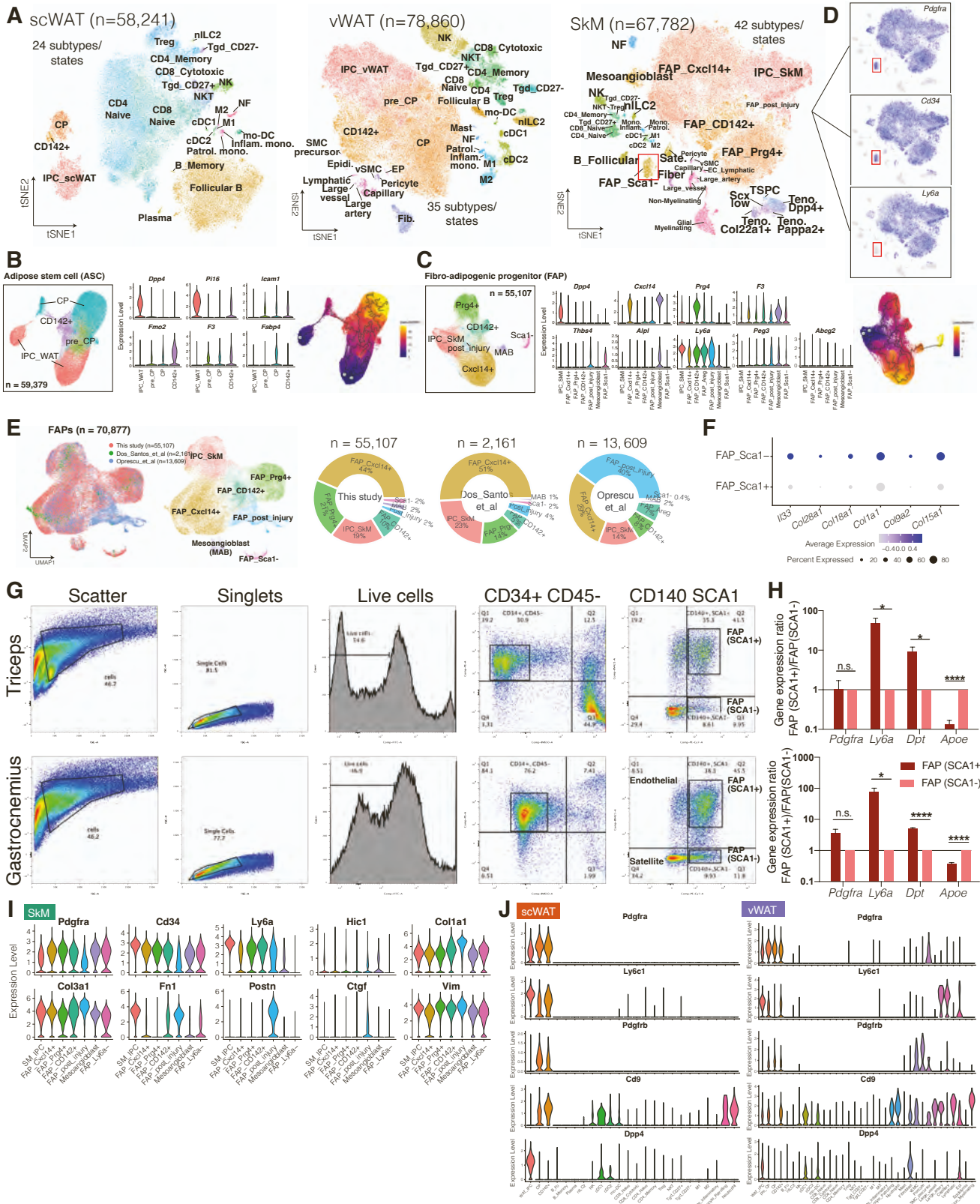


Figure S3. Single-cell subtype/state annotation in the three tissues and fibro-adipogenic progenitor validation and characterization in skeletal muscle (related to Figure 3). (A) Single-cell maps of scWAT, vWAT and SkM with cells coloured by cell subtype/state. (B and C) Cell states and pseudotime trajectory predictions of ASCs (B) and FAPs. (D) Single-cell map of SkM with cells coloured by *Pdgfra*, *Ly6a* and *Cd34* expression. (E) Re-clustering of FAPs from this study with FAPs from two publicly available datasets. The cells are coloured by study (left) and cell state (right). Proportions of the seven distinct FAP states in each study are shown below. (F) *Ii3* and collagen gene expression in *Sca1-* vs. *Sca1+* FAPs in our single-cell data. (G) FACS gating strategy and relative proportions of *Sca1+* and *Sca1-* FAP populations in triceps and gastrocnemius muscle. (H) Relative expression of positive and negative markers of *Sca1-* FAPs quantified using quantitative PCR. **P* < 0.05, ***P* < 0.01, ****P* < 0.001, *****P* < 0.0001 by unpaired t-test. n.s., not significant. Data are represented as mean ± SEM. (I) Marker gene expression in *Sca1+* and *Sca1-* FAPs, based on markers in Soliman et al. 2020. (J) Marker gene expression in all the cell types of scWAT and vWAT, based on markers in Shao et al. 2021 and Joffin et al. 2021. A list of abbreviations used in this figure appear in the Methods.

Figure S4

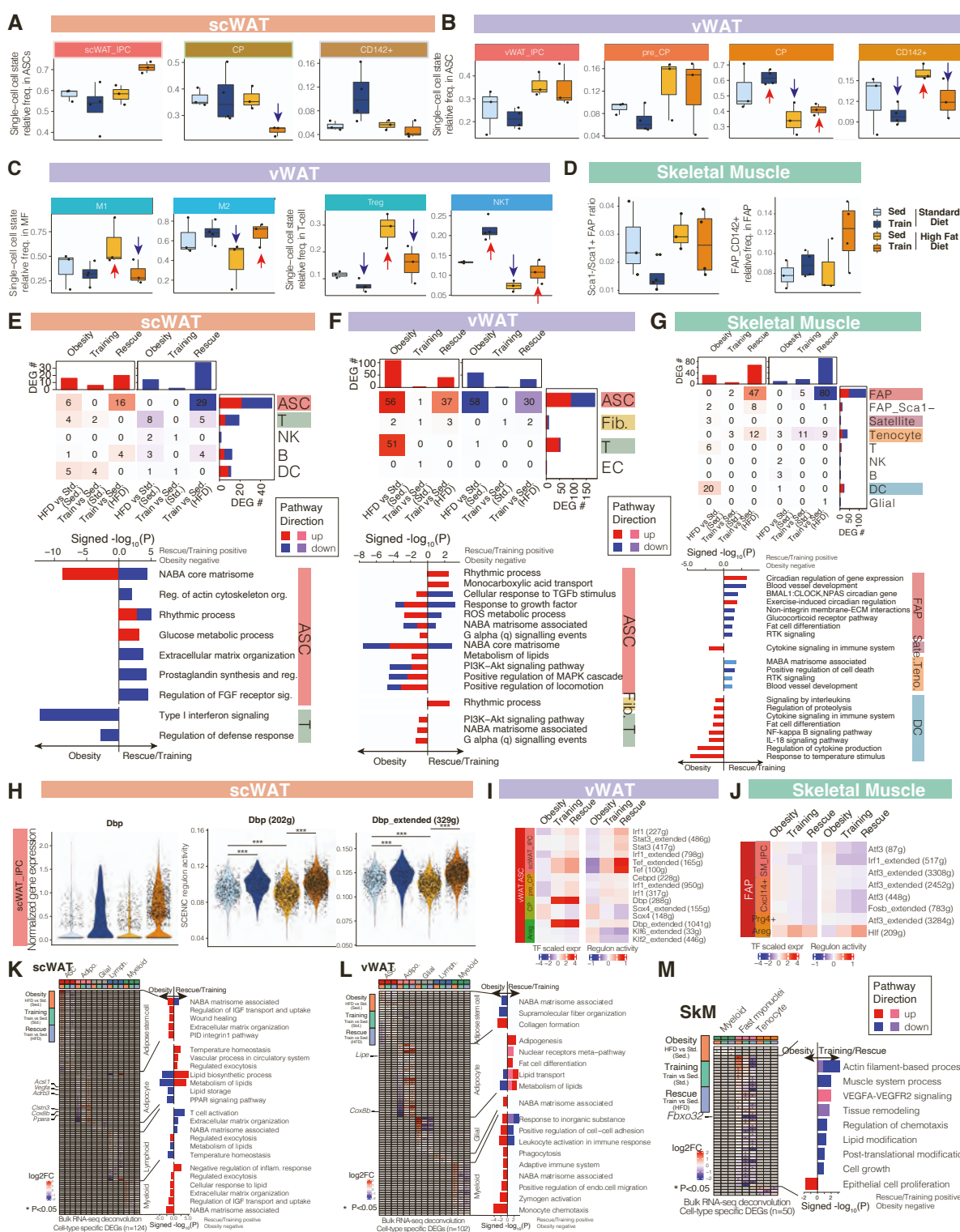


Figure S4. Cell state proportion, cell-type-specific transcriptomics, regulon activity and deconvolved transcriptomics changes with high-fat diet and exercise training (related to Figure 4). (A and B) Relative frequencies of ASC states in reference to all ASCs for each sample in scWAT (A) and vWAT (B). (C) Relative frequencies of M1 and M2 macrophages in all macrophages, and Tregs and NKT cells in all T-cells for each sample in vWAT. (D) Sca1⁺ FAP and Sca1⁻ FAP ratio, and relative frequencies of FAP_CD142⁺ in all FAPs for each sample in SkM. The boxplots are defined as Q1-1.5*IQR, Q1, median, Q3 and Q3+1.5*IQR. (E-G) The number of cell-type-specific DEGs (upper heatmap) that are up-regulated (red) or down-regulated (blue) in the three comparisons; and pathways (lower bar plot) that are significantly enriched in cell-type-specific DEGs in scWAT (E), vWAT (F), and SkM (G). X-axis of the bar plot shows -log₁₀p value with rescue/training pathways being positive, and obesity being negative. The bars are coloured by pathway direction in the three comparisons (red/pink: up-regulated, blue/purple, down-regulated). (H) Intervention group-specific Dbp expression and regulon activity in IPCs of scWAT. The number of genes regulated by Dbp is in parentheses. ***P < 0.001 by Wilcoxon Rank Sum Test. (I and J) Cell state-specific TF expression (left heatmap) and regulon activity (right heatmap) changes in the three comparisons in vWAT (I) and SkM (J). Only TF and regulon with p value less than 0.05 are shown. The number of genes regulated by each TF is in parentheses. (K-M) Deconvoluted cell group-specific DEGs (left heatmap) and pathways (right bar plot) that are up-regulated or down-regulated in our three comparisons in scWAT (K), vWAT (L) and SkM (M). The bar plots are formatted the same as panels E-G. A list of abbreviations used in this figure appear in the Methods.

Figure S5

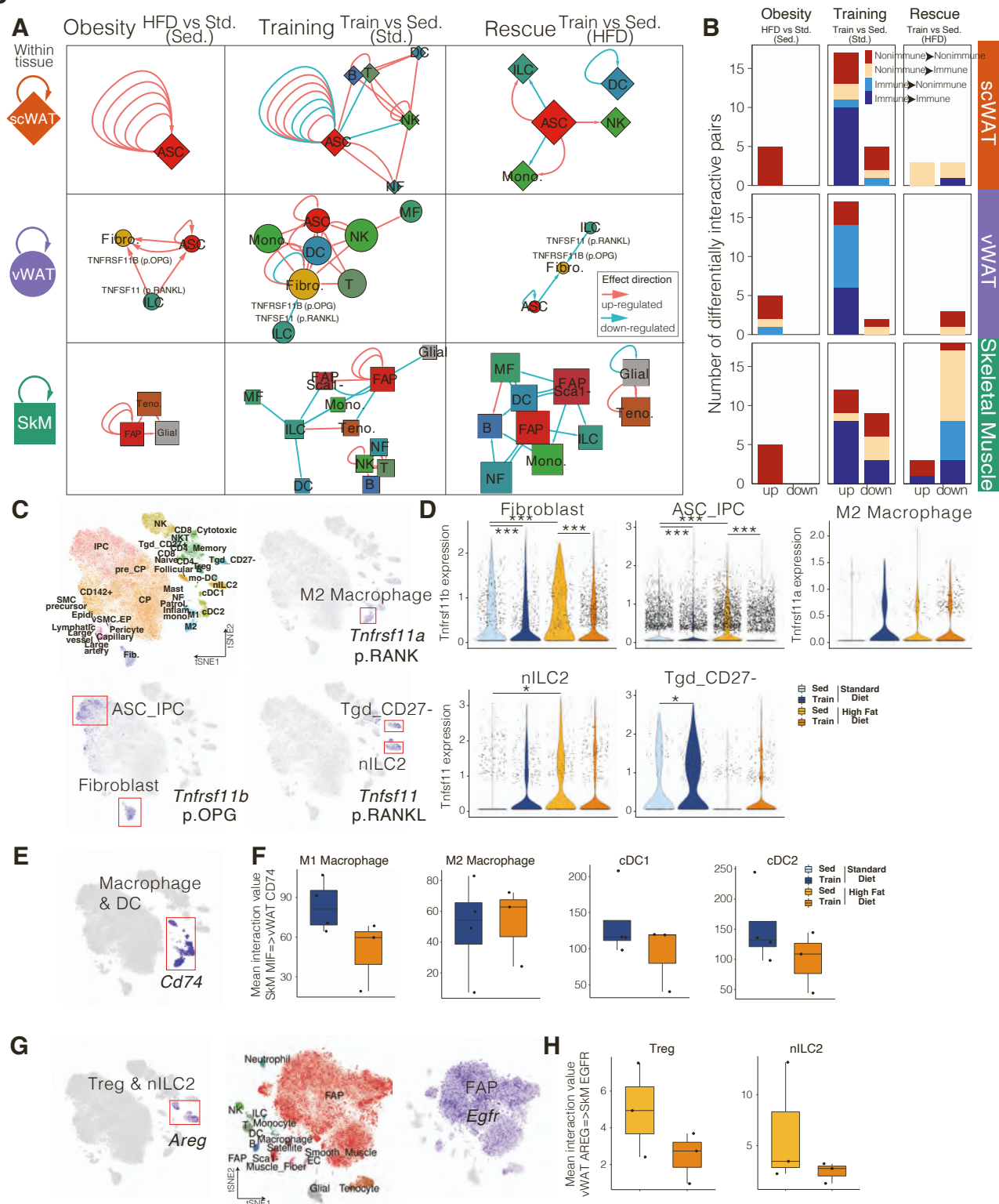


Figure S5. Within- and cross-tissue communication (related to Figure 5). (A) Within-tissue ligand-receptor networks across the three tissues and three comparisons at the cell-type level. Cell types (nodes) are shaped by tissue (diamond: scWAT, circle: vWAT, square: skeletal muscle) and sized by outdegree. Ligand-receptor interactions (edges) are directed, from ligand to receptor, and coloured by effect direction (pink: up-regulated, blue: down-regulated). (B) The number of differentially interactive ligand-receptor pairs that are up- and down-regulated across the three tissues and three comparisons at cell-type level. Each bar is coloured by if the ligand or the receptor is from an immune or non-immune cell type. (C, E and G) vWAT or SkM single-cell map with cells coloured by cell subtype/state, or expression of *Tnfsf11*, *Tnfrsf11a*, or *Tnfrsf11b* (C); *Cd74* (E); and *Areg* and *Egfr* (G). (D) Cell subtype/state-specific *Tnfsf11*, *Tnfrsf11a*, and *Tnfrsf11b* expression in the four intervention groups. * $P < 0.05$, *** $P < 0.001$ by Wilcoxon Rank Sum Test. (F and H) Interaction values between MIF in SkM and CD74 in dendritic cell (DC) and macrophage subtypes of vWAT (F) and between AREG in Treg and nILC2 of vWAT and EGFR in FAP of SkM (H). The boxplots are defined as $Q1-1.5 \cdot IQR$, $Q1$, median, $Q3$ and $Q3+1.5 \cdot IQR$. A list of abbreviations used in this figure appear in the Methods.

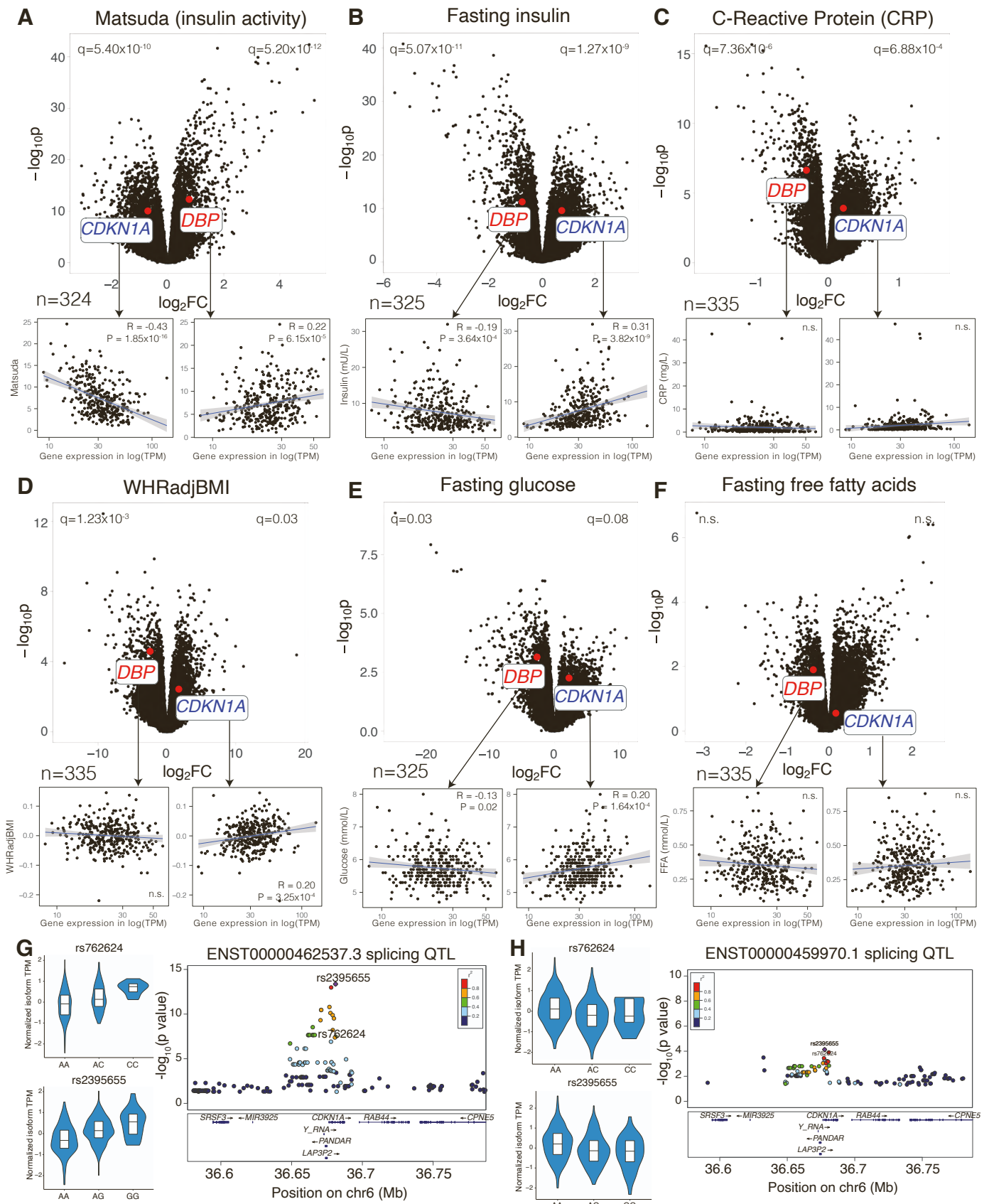
Figure S6

Figure S6. Association of DBP and CDKN1A with metabolic traits, and CDKN1A splicing QTLs in humans (related to Figure 6). (A-F) DBP and CDKN1A association with matsuda, an indicator of insulin activity (A); fasting insulin (B); CRP, an indicator of inflammation (C); waist hip ratio adjusted for BMI (D); fasting glucose (E); fasting free fatty acids (F) in scWAT of METSIM subjects. Genes (dots in upper plots) and subjects (dots in lower plots) are plotted. (G and H) Association of two SNPs (rs762624 and rs2395655) in CDKN1A with one transcript isoform (G) but not another (H) in METSIM. Violin plots show transcript levels associated with genotypes. Locus plots show splicing QTL p values and r-square values with nearby variants. TPM, reads mapped to transcript per million mapped reads.